The Astrophysical Journal, 938:83 (17pp), 2022 October 10 https://doi.org/10.3847/1538-4357/ac8c97
© 2022. The Author(s). Published by the American Astronomical Society.
OPEN ACCESS

Using 1991T/1999aa-like Type Ia Supernovae as Standardizable Candles

Jiawen Yang[1], Lifan Wang[1], Nicholas Suntzeff[1], Lei Hu[2], Lauren Aldoroty[1], Peter J. Brown[1], Kevin Krisciunas[1], Iair Arcavi[3], Jamison Burke[4,5], Lluís Galbany[6,7], Daichi Hiramatsu[8,9], Griffin Hosseinzadeh[10], D. Andrew Howell[4,5], Curtis McCully[4], Craig Pellegrino[4,5], and Stefano Valenti[11]

[1] George P. and Cynthia Woods Mitchell Institute for Fundamental Physics and Astronomy, Department of Physics and Astronomy, Texas A&M University, College Station, TX 77843, USA
[2] Purple Mountain Observatory, Nanjing 210023, People's Republic of China
[3] The School of Physics and Astronomy, Tel Aviv University, Tel Aviv 69978, Israel
[4] Las Cumbres Observatory, 6740 Cortona Drive, Suite 102, Goleta, CA, 93117-5575 USA
[5] Department of Physics, University of California, Santa Barbara, CA 93106-9530, USA
[6] Institute of Space Sciences (ICE, CSIC), Campus UAB, Carrer de Can Magrans, s/n, E-08193 Barcelona, Spain
[7] Institut d'Estudis Espacials de Catalunya (IEEC), E-08034 Barcelona, Spain
[8] Center for Astrophysics — Harvard & Smithsonian, 60 Garden Street, Cambridge, MA 02138-1516, USA
[9] The NSF AI Institute for Artificial Intelligence and Fundamental Interactions, USA
[10] Steward Observatory, University of Arizona, 933 North Cherry Avenue, Tucson, AZ 85721-0065, USA
[11] Department of Physics and Astronomy, University of California, Davis, 1 Shields Avenue, Davis, CA 95616-5270, USA
Received 2022 July 16; revised 2022 August 17; accepted 2022 August 22; published 2022 October 14

Abstract

We present the photometry of 16 91T/99aa-like Type Ia Supernovae (SNe Ia) observed by the Las Cumbres Observatory. We also use an additional set of 21 91T/99aa-like SNe Ia and 87 normal SNe Ia from the literature for an analysis of the standardizability of the luminosity of 91T/99aa-like SNe. We find that 91T/99aa-like SNe are 0.2 mag brighter than normal SNe Ia, even when fully corrected by the light-curve shapes and colors. The weighted rms of the 91T/99aa-like SNe (with $z_{\rm CMB} > 0.01$) Hubble residuals is 0.25 ± 0.03 mag, suggesting that 91T/99aa-like SNe are also excellent relative distance indicators to ±12%. We compare the Hubble residuals with the pseudo-equivalent width (pEW) of Si II $\lambda\lambda$6355 around the date of maximum brightness. We find that there is a broken linear correlation between those two measurements for our sample including both 91T/99aa-like and normal SNe Ia. As the $\mathrm{pEW_{max}}$(Si II $\lambda\lambda$6355) increases, the Hubble residual increases when $\mathrm{pEW_{max}}$(Si II $\lambda\lambda$6355) < 55.6 Å. However, the Hubble residual stays constant beyond this. Given that 91T/99aa-like SNe possess shallower Si II lines than normal SNe Ia, the linear correlation at $\mathrm{pEW_{max}}$(Si II $\lambda\lambda$6355) < 55.6 Å can account for the overall discrepancy of Hubble residuals derived from the two subgroups. Such a systematic effect needs to be taken into account when using SNe Ia to measure luminosity distances.

Unified Astronomy Thesaurus concepts: Supernovae (1668); Type Ia supernovae (1728)

Supporting material: machine-readable tables

1. Introduction

Type Ia supernovae (SNe Ia) have played an important role in modern cosmology as cosmological distance indicators, which led to the discovery of the accelerating expansion of the universe and ever-improving values of the Hubble constant (Hamuy et al. 1996a; Riess et al. 1998; Perlmutter et al. 1999; Suntzeff et al. 1999; Freedman et al. 2001; Riess et al. 2021). Although they are not perfect standard candles, their luminosities can be calibrated using light-curve shapes and colors of SNe Ia (e.g., see Phillips 1993; Riess et al. 1996; Hamuy et al. 1996b; Phillips et al. 1999), by means of which the precision of the distance determination can be improved to 5%–10%.

It is generally agreed that SNe Ia result from the thermonuclear runaway of a carbon-oxygen (CO) white dwarf (WD) accreting mass from a companion star in a binary system while the nature of the companion star remains unclear. Potential progenitor systems can be broadly categorized into two groups: single degenerate (SD), where the companion star is a main-sequence, subgiant, red giant, or helium star, and double degenerate (DD), where the companion star is another WD. Within this scheme, three major triggering mechanisms have been proposed. The explosion can be triggered by compressional heating near the WD center as a deflagration front as the WD accretes matter from a degenerate or nondegenerate companion to a mass close to the Chandrasekhar limit (e.g., Whelan & Iben 1973). The explosion can also be triggered by the heat of the dynamical merging process of two CO WDs in a binary system with angular momentum loss via gravitational radiation (e.g., Iben & Tutukov 1984; Webbink 1984). Another triggering mechanism is through the detonation of a layer of helium on the surface of the WD, which causes a detonation front propagating inwards the WD (e.g., Taam 1980; Woosley & Weaver 1994).

Despite the homogeneity assumed for corrected peak luminosities in these SNe, there remains a persistent intrinsic scatter among SNe Ia beyond just photometric error and the uncertainties in the reddening law, both photometrically and spectroscopically. Mounting evidences are revealed by the spectral diversity among SNe Ia. It is clear that they are not identical standard candles and are most likely to originate from more than one explosion mechanism as studied in the literature. Overall, SNe Ia have been classified into four major subgroups

Original content from this work may be used under the terms of the Creative Commons Attribution 4.0 licence. Any further distribution of this work must maintain attribution to the author(s) and the title of the work, journal citation and DOI.

based on their maximum light spectra: core-normal, shallow-silicon, cool, and broad line (Branch et al. 2006; Burrow et al. 2020). They are also grouped into different categories based on the evolution of the Si II $\lambda\lambda$ 6355 velocities (Benetti et al. 2005; Wang et al. 2009). There are other frequently used subtypes based on the observed spectral features. The representative examples include (1) the luminous 91T-like SNe, which show weak features of intermediate-mass elements (IMEs) and prominent Fe II/Fe III lines (Phillips et al. 1992; Filippenko et al. 1992a); (2) the subluminous 91bg-like (Filippenko et al. 1992b; Leibundgut et al. 1993) characterized by strong features of IMEs and prominent Ti II lines; (3) the 02cx-like SNe (Li et al. 2003) showing weak Si II lines before maximum light similar to that of 91T-like SNe but with 91bg-like luminosity and significantly lower ejecta velocities than 91T-like SNe; (4) the overluminous 03fg-like SNe (Scalzo et al. 2012; Howell et al. 2006) with strong absorption lines due to unburned carbon in their spectra, which could be identified with explosions of super-Chandrasekhar mass WDs; and (5) the so-called SNe Ia-CSM 02ic-like (Hamuy 2003), which show strong, broad emission lines of hydrogen presumably caused by strong interaction with circumstellar matter.

The 99aa-like SNe are similar to the 91T-like SNe with the subtle difference of having weak Ca II H&K and Si II absorption lines before maximum light. Their premaximum spectral evolution is intermediate between 91T-like SNe Ia and normal SNe Ia (Krisciunas et al. 2000; Garavini et al. 2004). Whether 91T-like SNe are extreme events of SNe Ia or together with 99aa-like SNe they form a separate class arising from systematically different progenitors is still unknown. In this paper, we consider them together as 91T/99aa-like SNe Ia. So far, cosmological studies using SNe Ia usually exclude spectroscopically peculiar SNe Ia including 91T/99aa-like SNe Ia. However, the intrinsic rate of peculiar SNe Ia can be as high as 36%, with ~20% being 91T/99aa-like SNe Ia (Li et al. 2001). Since they are among the most luminous SNe Ia and are located in regions with comparatively young stars (Hamuy et al. 1996b), future flux-limited surveys such as LSST/Rubin, WFIRST/Roman, and JWST will inevitably be biased toward finding this class. A potential Malmquist bias then becomes one of the critical issues for these future surveys if the luminosities are not properly taken into account. Not only are 91T/99aa-like objects more luminous, previous studies have also shown that Hubble residuals of 91T/99aa-like objects are on average brighter than the residuals of normal SNe Ia even after light-curve shape and color corrections (Reindl et al. 2005; Boone et al. 2021). Understanding the intrinsic properties of these SNe Ia is crucial to mitigate inevitable systematic errors in supernova cosmology.

In this paper, we present the photometry of 16 91T/99aa-like SNe observed extensively in $Bg'Vr'i'$ as part of the Las Cumbres Observatory (Brown et al. 2013) Supernova Key Project and Global Supernova Project. Together we gather 21 91T/99aa-like objects (as well as additional data of our Las Cumbres 91T/99aa-like object SN 2016hvl) and 87 normal SNe Ia from the literature. With this sample, we analyze the standardizability of 91T/99aa-like objects as relative distance indicators and search for potential systematic effects that may bias the cosmological measurement. The remainder of this paper is organized as follows. In Section 2, we present the photometric observations, data reduction, calibration, and light-curve-fitting techniques. The spectral and line strength calculations of Si II$\lambda\lambda$6355 are presented in Section 3. In Section 4 we introduce the method to standardize the peak luminosity of SNe Ia. In Section 5 we present the residual Hubble diagram made with our sample and the use of Si II$\lambda\lambda$6355 for distance measurements. The paper concludes with a summary and discussion in Section 6. Throughout this paper, we assume a Hubble constant of $H_0 = 72\,\mathrm{km\,s^{-1}/Mpc}$ and a standard cosmology of $\Omega_M = 0.28$, $\Omega_\Lambda = 0.72$.

2. Photometry

2.1. Data

2.1.1. Las Cumbres Data

Here we adopt a loose classification scheme of 91T/99aa-like SNe, where an SN Ia is classified as 91T/99aa-like as long as it is reported as a 91T/99aa-like object by at least one source (listed in Tables 1 and 2) in the literature. As will be shown later in this paper, the definition of 91T/99aa-like SNe can be replaced by a more quantitative scheme, and the results of our analysis will not be affected by this initial classification.

The general properties of our 16 Las Cumbres Observatory 91T/99aa-like SNe are given in Table 1. The Las Cumbres Observatory operates a fleet of 1 m class telescopes distributed around the globe. Las Cumbres Observatory images were preprocessed by the BANZAI pipeline (McCully et al. 2018) (after 2016 June) and ORAC pipeline (before 2016 June), during which bad pixel masking, bias subtraction, dark subtraction, and flat-field correction are done. Most SNe in the sample are located in the vicinity of their host-galaxy nuclei. Without template subtraction, the galaxy background with nonuniform brightness can significantly degrade the photometric accuracy. To remove the galaxy background contamination, we subtract a reference image in the same passband for each exposure of the SN. Since the pre-explosion observations are generally unavailable for Las Cumbres Observatory telescopes, we adopt the observations taken after the SNe have sufficiently faded (typically more than one year after explosion) to create the reference image. More specifically, the late-time observations are coadded and subsequently aligned to the science frame using SWarp (Bertin et al. 2002). We use the Saccadic Fast Fourier Transform algorithm (SFFT hereafter; Hu et al. 2021) to perform the galaxy subtractions. The SFFT method is a novel approach that presents the question of image subtraction in the Fourier domain, which brings a significant computational speed-up by leveraging GPU acceleration. Unlike the widely used HOTPANTS image subtraction program, SFFT uses a delta function basis that allows for kernel flexibility and requires minimal user-adjustable parameters. In our work, SFFT successfully carries out the galaxy subtraction for all images with the default software configuration (see SFFT GitHub[12]). By contrast, Baltay et al. (2021) found that HOTPANTS produced satisfactory subtractions only for two-thirds of SNe in their sample observed by Las Cumbres Observatory in their work.

For precision photometry, a small stamp centered at the SN position (typically 200 pixels × 200 pixels) is cut out from the difference image and pasted back to the original science image. The cutout stamp is added with a constant background to match the background level of the science image. Point spread function (PSF) photometry is then done on the new set of

[12] https://github.com/thomasvrussell/sfft

Table 1
General Properties of Las Cumbres 91T/99aa-like Supernovae

SN Name	α(2000)[a]	δ(2000)[a]	Host Galaxy[a]	z_{helio}[b]	Discovery Reference	Spectroscopic Reference
SN 2014dl	16:29:46.09	+08:38:30.6	UGC 10414	0.03297	CBET 3995	CBET 3995
SN 2014eg	02:45:09.27	−55:44:16.9	ESO 154–G10	0.01863	CBET 4062	CBET 4062
PS 15sv	16:13:11.74	+01:35:31.1	⋯	0.033	ATEL 7280	ATEL 7308
LSQ 15aae	16:30:15.70	+05:55:58.7	2MASX J16301506+0555514[c]	0.0516[c]	LSQ	ATEL 7325
SN 2016gcl	23:37:56.62	+27:16:37.7	AGC 331536	0.028	TNSTR-2016-644	TNSCR-2016-655
SN 2016hvl	06:44:02.16	+12:23:47.8	UGC 3524	0.01308	TNSTR-2016-884	TNSCR-2016-892
SN 2017awz	11:07:35.50	+22:51:04.7	SDSS J110735.46+225104.2	0.02222	TNSTR-2017-200	TNSCR-2017-210
SN 2017dfb	15:39:05.04	+05:34:17.0	ARK 481	0.02593	TNSTR-2017-449	TNSCR-2017-476
SN 2017glx	19:43:40.30	+56:06:36.4	NGC 6824	0.01183	TNSTR-2017-963	TNSCR-2017-970
SN 2017hng	04:21:40.58	−03:32:26.5	2MASX J04214029–0332267	0.039	TNSTR-2017-115	TNSCR-2017-117
SN 2018apo	12:45:05.30	−44:00:23.0	ESO 268-G 037	0.01625	TNSTR-2018-440	TNSCR-2018-468
SN 2018bie	12:35:44.33	−00:13:16.0	⋯	0.022	TNSTR-2018-609	TNSCR-2018-626
SN 2018cnw	16:59:05.06	+47:14:11.0	⋯	0.02416	TNSTR-2018-832	TNSCR-2018-833
SN 2019dks	11:44:05.59	−04:40:25.3	⋯	0.057	TNSTR-2019-566	TNSCR-2019-601
SN 2019gwa	15:58:41.18	+11:14:25.1	⋯	0.054988	TNSTR-2019-930	TNSCR-2019-965
SN 2019vrq	03:04:21.46	−16:01:26.4	GALEXASC J030421.67–160124.7	0.01308	TNSTR-2019-247	TNSCR-2019-248

Notes.
[a] Basic information for each SN, including its J2000 R.A. and decl., and its host galaxy, were sourced from TNS or the discovery references.
[b] Host-galaxy heliocentric redshifts are from the NASA/IPAC Extragalactic (NED) or TNS Database unless otherwise indicated.
[c] Phillips et al. (2019).

Table 2
General Properties of 91T/99aa-like SNe Ia in the Literature

SN Name	Host Galaxy	z_{helio}[a]	Photometry Reference	Classification Reference
SN 1991T	NGC 4527	0.00579	1	IAUC 5239
SN 1995bd	UGC 3151	0.0146	2	IAUC 6278
SN 1998ab	NGC 4704	0.02715	4	IAUC 7054
SN 1998es	NGC 632	0.01057	4, 5	IAUC 7054
SN 1999aa	NGC 2595	0.01446	4, 5	IAUC 7108
SN 1999ac	NGC 6063	0.0095	4, 5	IAUC 7122
SN 1999aw	Anon 1101–06	0.0379[6]	8	7
SN 1999dq	NGC 976	0.01433	4, 5	IAUC 7250
SN 1999gp	UGC 1993	0.02675	4, 5	7
SN 2001V	NGC 3987	0.01502	5, 6	7
SN 2001eh	UGC 1162	0.03704	5, 6	7
SN 2002hu	MCG +06-6-12	0.0374[9]	6	7
SN 2003fa	ARK 527	0.039[5]	5, 6	7
SN 2004br	NGC 4493	0.02308	5	10
SN 2005M	NGC 2930	0.022[5]	5, 6, 11	IAUC 8474
SN 2005eq	MCG -01-9-6	0.02891	5, 6, 11	7
SN 2005hj	SDSS J012648.45–011417.3	0.05738	6, 11	7
SN 2007S	UGC 5378	0.01385	6, 11, 12	CBET 839
SN 2007cq	2MASX J22144070+0504435	0.02604	5, 6, 12	7
SN 2011hr	NGC 2691	0.01339	13	CBET 2901
SN 2016hvl	UGC 3524	0.01308	14, 15, 16	ATEL 9720
iPTF 14bdn	UGC 8503	0.01558	12, 17	17

Note. (1) Lira et al. (1998); (2) Riess et al. (1999); (3) Altavilla et al. (2004); (4) Jha et al. (2006); (5) Ganeshalingam et al. (2010); (6) Hicken et al. (2009); (7) Blondin et al. (2012); (8) Strolger et al. (2002); (9) Blondin et al. 2012; (10) Silverman et al. (2012); (11) Krisciunas et al. (2017); (12) Brown et al. (2014); (13) Zhang et al. (2016); (14) Stahl et al. (2019); (15) Foley et al. (2018); (16) Baltay et al. (2021); (17) Smitka et al. (2015).
[a] Heliocentric redshift is taken from the NASA/IPAC Extragalactic Database (NED) unless indicated otherwise.

images with pasted stamps using DAOPHOT (Stetson 1987). We first run ALLSTAR on each frame separately to generate the entire star list for each frame. Then, the instrumental magnitudes for images taken with the same filter for the same object are solved simultaneously using ALLFRAME. To do so, the coordinate transformations between the images are found by DAOMATCH and refined by DAOMASTER. Then, ALLFRAME performs simultaneous profile fits for all stars in given images while maintaining a consistent star list and their positions for all images. Rather than solving for an independent position for each star in each image like in ALLSTAR, ALLFRAME solves for a single position for each star and transforms that to the coordinate system of other images using the transformations found by DAOMASTER. This way, the star's

Table 3
Las Cumbres 91T/99aa-like SNe Photometry in Natural Systems

SN	Filter	MJD	Magnitude	Magnitude Error	Site, Telescope, and Instrument
SN 2014dl	*B*	56929.3814	16.473	0.053	coj1m003-kb71
SN 2014dl	*B*	56929.3839	16.473	0.058	coj1m003-kb71
SN 2014dl	*B*	56932.3744	16.303	0.057	coj1m011-kb05
SN 2014dl	*B*	56932.3769	16.292	0.056	coj1m011-kb05
SN 2014dl	*B*	56935.0704	16.272	0.044	elp1m008-kb74
SN 2014dl	*B*	56937.0705	16.299	0.054	elp1m008-kb74
SN 2014dl	*B*	56937.073	16.309	0.053	elp1m008-kb74
SN 2014dl	*B*	56940.0746	16.432	0.045	elp1m008-kb74
SN 2014dl	*B*	56940.0771	16.436	0.043	elp1m008-kb74
SN 2014dl	*B*	56942.0803	16.544	0.05	elp1m008-kb74

(This table is available in its entirety in machine-readable form.)

centroid, especially the centroid of the SN of interest when the SN becomes dimmer, can be better determined and results in higher photometric precision. Without a common position, the fainter photometry is biased brighter as the centroiding algorithm will tend toward peaks due to low signal to noise in the PSF location.

Photometric measurements are calibrated by means of field stars in the APASS catalog DR9 (Henden et al. 2016) with catalog magnitudes in the range $10\,\mathrm{mag} < m < 18\,\mathrm{mag}$ and uncertainties $\Delta m \leqslant 0.1\,\mathrm{mag}$ in each calibration band. The APASS catalog calibration was done using Landolt and SDSS standard stars. Therefore, the Las Cumbres Observatory magnitudes presented here are based on the Vega standard system for *B* and *V*, and the Sloan BD17 system for $g'r'i'$ commonly called AB magnitudes. Photometric coefficients appropriate to the Las Cumbres Observatory 1 m telescopes (see Table B1 in Valenti et al. 2016) were used to convert APASS catalog magnitudes to values in the Las Cumbres Observatory natural system. We use the color terms to convert the APASS magnitude to Las Cumbres Observatory natural system magnitude as follows:

$$m_{\mathrm{nat}} = m_{\mathrm{APASS}} + C \times \mathrm{color}, \quad (1)$$

where m_{nat} is the natural system magnitude, m_{APASS} is the APASS magnitude, and *C* and "color" are the appropriate color term and color for each filter.[13] Zero-points for each exposure were then determined by the difference between instrumental magnitudes of field stars and the corresponding APASS magnitudes converted to the Las Cumbres Observatory natural system. After that, the SN natural system photometry is brought onto standard systems using S-corrections (see Section 2.2). Final photometry data (both in the natural system and in the standard system) are given in Tables 3 and 4. Light curves are shown in Figure 1 together with light-curve fits (see Section 2.3). Photometry in *U* and *R* filters without color term corrections and S-corrections is also provided in Table 5 for completeness.

[13] APASS DR9 does not contain any *U*- or *R*-band magnitudes. We have *U* and *R* data for three objects. For completeness, here we use the transformation given by Jordi et al. (2006) to derive the *U* and *R* magnitudes of reference stars from filters with known magnitudes. Also, note that Valenti et al. (2016) did not provide color terms for *U* and *R*. Thus, we did not convert the magnitudes of reference stars to the natural system.

Table 4
Las Cumbres 91T/99aa-like SNe Photometry in Standard Systems

SN	Filter	MJD	Magnitude	Magnitude Error
SN 2014dl	*B*	56929.3814	16.458	0.057
SN 2014dl	*B*	56929.3839	16.458	0.061
SN 2014dl	*B*	56932.3744	16.287	0.06
SN 2014dl	*B*	56932.3769	16.276	0.059
SN 2014dl	*B*	56935.0704	16.255	0.048
SN 2014dl	*B*	56937.0705	16.281	0.058
SN 2014dl	*B*	56937.073	16.291	0.057
SN 2014dl	*B*	56940.0746	16.413	0.049
SN 2014dl	*B*	56940.0771	16.418	0.047
SN 2014dl	*B*	56942.0803	16.527	0.055

(This table is available in its entirety in machine-readable form.)

2.1.2. ANDICAM Data

In Table 6 we present complementary *BV* photometry for two objects, SN 2019dks and SN 2018bie, obtained under programs NOAO-18A-0047, NOAO-18B-0016, and NOAO-19A-0081 with the A Novel Double Imaging Camera (ANDICAM; DePoy et al. 2003) instrument mounted on the 1.3 m telescope and operated by the SMARTS Consortium at the Cerro Tololo Inter-American Observatory (CTIO). Images were reduced by the SMARTS consortium using standard routines and were retrieved from their FTP server. Photometry on the reduced images was performed following standard procedures. Aperture photometry was performed on the SN and field stars, and then the instrumental magnitudes of the stars were calibrated to the APASS catalog; once the magnitude conversion was found, we applied ANDICAM color terms and applied an airmass correction to find the SN magnitude in each image.

2.1.3. Data from the Literature

To supplement our 91T/99aa-like SNe sample, we gathered all SNe Ia that are classified as 91T/99aa-like[14] from at least one source and have at least one *B*-band data point in the Open Supernova Catalogue (Guillochon et al. 2017). Then, we make the quality cut following these criteria: (1) *B* and *V* data must be present; (2) at least one band of *i*, *R*, and *I* must have data (in order to calculate K-corrections in the *V*-band (see

[14] SN 2013dh is excluded, as it is a possible Iax SN (see ATEL 5143). SN1997br is also excluded due to bad light-curve fits.

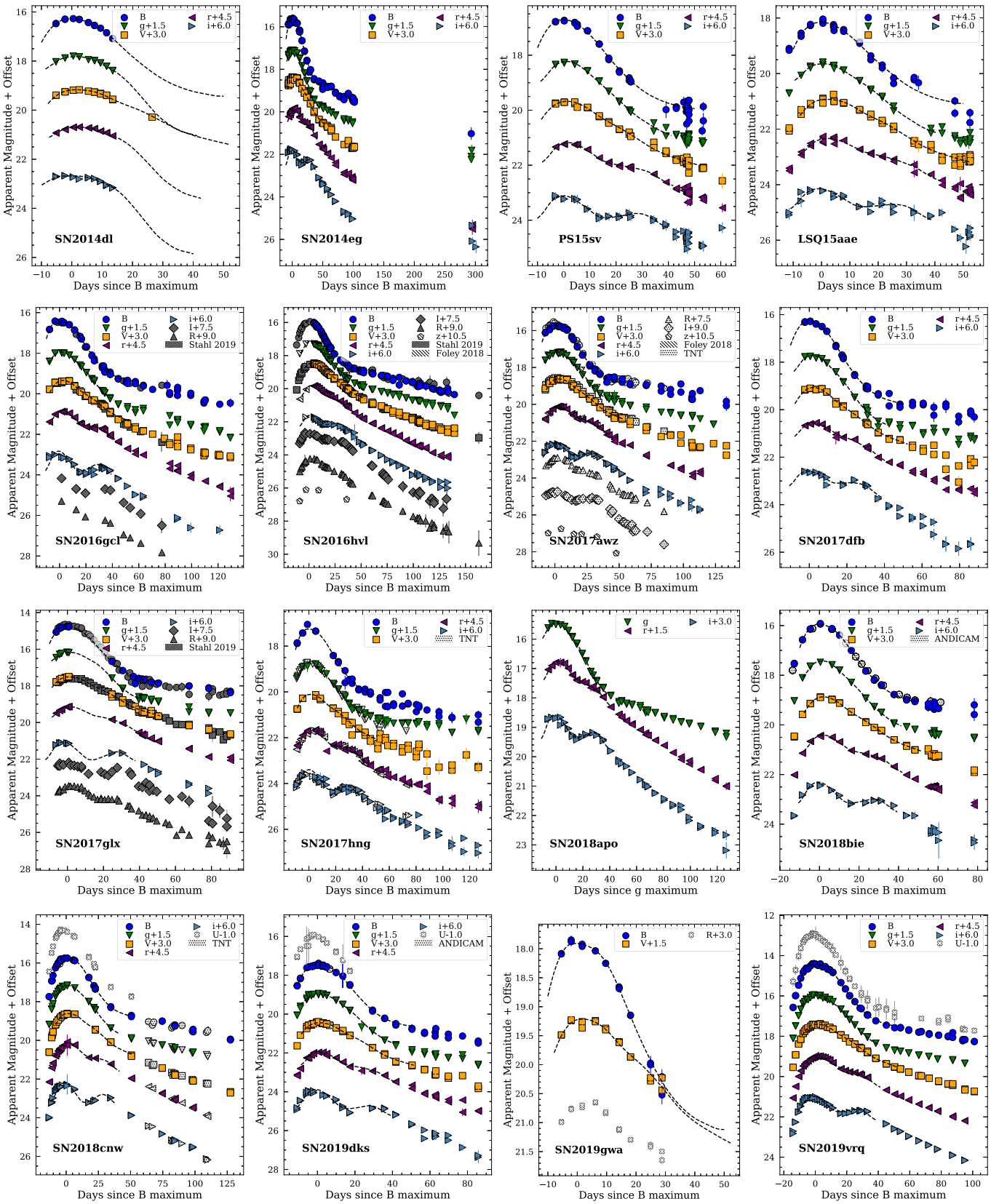

Figure 1. Light curves of Las Cumbres Observatory 91T/99aa-like SNe in natural systems. Light-curve fits for $BVg'r'i'$ bands using FPCA (He et al. 2018) are shown as dashed lines overlaid on top of their corresponding data points. For completeness, we also plot U and R photometry when available, though for those two filters, we did not correct for color terms. For SNe with data from non–Las Cumbres observing programs, they are included in the figure for comparison, with the sources of the data shown in the insert legends at the upper-right corner of each panel. The relevant references are Stahl 2019: Stahl et al. (2019), Foley 2018: Foley et al. (2018), and TNT: Tsinghua-NAOC Telescope.

Table 5
Las Cumbres 91T/99aa-like SNe Photometry in *UR* Bands

SN	Filter	MJD	Magnitude	Magnitude Error	Site, Telescope, and Instrument
SN 2018cnw	*U*	58287.365	17.436	0.074	elp1m008-fl05
SN 2018cnw	*U*	58287.3712	17.447	0.061	elp1m008-fl05
SN 2018cnw	*U*	58289.3094	16.48	0.08	elp1m008-fl05
SN 2018cnw	*U*	58289.3134	16.479	0.058	elp1m008-fl05
SN 2018cnw	*U*	58290.3227	16.137	0.085	elp1m008-fl05
SN 2018cnw	*U*	58290.3267	16.145	0.086	elp1m008-fl05
SN 2018cnw	*U*	58292.3054	15.707	0.073	elp1m008-fl05
SN 2018cnw	*U*	58292.3094	15.706	0.083	elp1m008-fl05
SN 2018cnw	*U*	58293.157	15.588	0.111	elp1m008-fl05
SN 2018cnw	*U*	58293.161	15.642	0.059	elp1m008-fl05

(This table is available in its entirety in machine-readable form.)

Table 6
ANDICAM SN Photometry in Standard Systems

SN	MJD	Filter	Magnitude	Magnitude Error
SN 2018bie	58251.0668	*B*	17.802	0.067
SN 2018bie	58261.1015	*B*	16.123	0.026
SN 2018bie	58271.0232	*B*	16.146	0.062
SN 2018bie	58278.0392	*B*	16.713	0.029
SN 2018bie	58283.004	*B*	17.251	0.053
SN 2018bie	58285.9925	*B*	17.548	0.066
SN 2018bie	58289.0281	*B*	17.819	0.034
SN 2018bie	58292.985	*B*	18.129	0.08
SN 2018bie	58296.9623	*B*	18.408	0.035
SN 2018bie	58304.9651	*B*	18.781	0.052
SN 2018bie	58308.9624	*B*	18.9	0.1
SN 2018bie	58312.9721	*B*	19.007	0.082
SN 2018bie	58320.954	*B*	19.055	0.175
SN 2018bie	58325.9612	*B*	19.092	0.118
SN 2019dks	58595.1002	*B*	17.543	0.046
SN 2019dks	58597.0843	*B*	17.48	0.054
SN 2019dks	58600.05	*B*	17.532	0.056
SN 2019dks	58602.0576	*B*	17.57	0.048
SN 2019dks	58604.1016	*B*	17.679	0.053
SN 2019dks	58595.1097	*V*	17.49	0.049
SN 2019dks	58597.0938	*V*	17.411	0.034
SN 2019dks	58600.0595	*V*	17.466	0.042
SN 2019dks	58602.0681	*V*	17.498	0.053
SN 2019dks	58604.1111	*V*	17.583	0.05

Section 2.4)); (3) for the above three bands, there must be at least one data point after 15 days postmaximum (to ensure a good light-curve fit); and (4) for the above three bands, there must be at least six data points observed in each band. After making the cuts, we are left with 21 91T/99aa-like objects. Their general properties are listed in Table 2.

To compare 91T/99aa-like SNe with normal SNe Ia, we include normal SNe Ia from Jha et al. (2006), Hicken et al. (2009, 2012), Ganeshalingam et al. (2010), and Stahl et al. (2019). All of the above papers provide photometry data in the standard system, so no further S-correction is needed (see Section 2.2). Data are further selected according to the same criteria in the above paragraph, with extra criteria: For each of the three bands mentioned above, there must be at least two data points before maximum, and we tighten the constraint on the minimum total number of data points in each band from six to eight. After applying these requirements, we are left with 87 normal SNe Ia.

2.2. S-corrections

Photometric systems of different telescope and instrument combinations never match exactly. Since we try to compare the photometry of SNe taken by different instruments, each one of which defines its own photometric system, it is necessary to transform all of the data to a common standard system. Although the color equations are meant to transform between natural system magnitudes and standard system magnitudes, they lose accuracy when transforming natural system magnitudes of SNe to the standard system, as color terms are derived from stellar objects while the spectral energy distributions (SEDs) of SNe are quite different from stellar spectra. This problem is mitigated through the use of S-corrections (Stritzinger et al. 2002; Krisciunas et al. 2003).

S-corrections specifically account for differences in filter band passes for nonstellar objects. The magnitude correction is calculated by finding the difference between the synthetic photometry generated by integrating the spectra or spectral templates in the old system and new systems:

$$S_{s,\mathrm{corr}} = m_{s,\mathrm{standard}} - m_{s,\ \mathrm{natural}}\ , \tag{2}$$

where $S_{s,\mathrm{corr}}$ is the photometric S-correction in magnitudes in filter s, $m_{s,\mathrm{standard}}$ is the synthetic photometry of the object's SED using the standard filter bandpass, and $m_{s,\mathrm{natural}}$ is the synthetic magnitude calculated using the natural filter bandpass. Thus, passbands $S(\lambda)$ of the two systems and the SED at each photometric epoch are both needed to calculate S-corrections. For our Las Cumbres Observatory instrumental system, we use the filter transmission curves and quantum efficiencies given by Baltay et al. (2021). For the standard band passes, we adopt filter functions given by Bessell (1990) for *BVRI* and Fukugita et al. (1996) for $g'r'i'$. Since we do not have spectra at all photometry epochs, we use spectral templates from Hsiao et al. (2007) and color match them with observed photometry using the same method described in Section 2.4. We use those as our SED approximations for our sample. These spectral templates only cover −19 to 70 days with respect to the *B*-band maximum. For data outside this range, we simply use the earliest or latest SED as the SED approximations for data points earlier/later than the range.

2.3. Light-curve-fitting Technique

Direct measurements of the peak magnitudes and the 15 day decline rates ($\Delta m_{15}(B)$) are uncertain for most SN Ia light curves because the lack of high-cadence photometric observations. Thus, different models have been used to fit the discrete light curves (e.g., the light-curve stretch method, Goldhaber et al. 2001; MLCS, Riess et al. 1996, and SNooPy Burns et al. 2011). Here we use the functional principal component analysis (FPCA) template-fitting technique introduced by He et al. (2018). The light curves in each band are fitted as follows:

$$m(t - t_0) = m_0 + \phi_0(t - t_0) + \sum_{i=1}^{K} \beta_i \phi_i(t - t_0) , \quad (3)$$

where $m(t - t_0)$ is the magnitude at time t in a specific band, t_0 is the time of maximum light, and m_0 is the maximum magnitude. The functions ϕ_i for $i = 0$ to K are templates constructed from a collection of well-observed SN Ia light curves, where ϕ_0 is the mean template that captures the general light-curve shape, and ϕ_i for $i = 1$ to K is the K fixed principal component templates that capture any additional variations of the observed light curves from the mean function ϕ_0. Lower-order functions of ϕ_i capture more variability (He et al. 2018).

Two types of templates were introduced in He et al. (2018). One is "filter-specific templates," where the templates for each filter were trained with data only in that filter. The other is "filter-vague templates," where the templates were trained with data from all filters (*BVRI*) together. Since He et al. (2018) only introduced the filter-specific templates for *BVRI* filters, in this work, filter-specific templates were used for the B and V bands and filter-vague templates were used for the $g'r'i'$ bands. The first two principal components account for more than 90% of the variability of the light curves (see Figure 1 in He et al. 2018). So we only use the first two principal components to fit the light curves. The light curve is then fully parameterized by (m_0, t_0, β_1, β_2) in our case. The best coefficients are found by minimizing χ^2 using the least-squares fitting package `pycmpfit`,[15] with additional constraints that the fitted light curve must monotonically increase before maximum and monotonically decrease 35 days after maximum. $\Delta m_{15}(B)$ is then measured from the fitted light curves (for error calculation on $\Delta m_{15}(B)$, see the Appendix in L. N. Aldoroty et al. 2022, in preparation). The fitted parameters and measured $\Delta m_{15}(B)$ are listed in Tables 7 and 8.

2.4. K-corrections

To compare the photometry of SNe at different redshifts, K-corrections are needed to account for the effect of the redshift on the observed magnitudes (Hamuy et al. 1993; Kim et al. 1996).

Before we calculate and apply the K-correction to the observed photometric light curves, the light curves are first corrected for extinction along the line of sight in the Milky Way (MW) using the MW dust map given by Schlegel et al. (1998), assuming the MW $R_V = 3.1$ and a Fitzpatrick (1999) reddening law. Then the light curves are further corrected by removing the time dilation due to Hubble expansion. Corrected light curves are then fitted using the FPCA light-curve-fitting technique described above. The time of the B-band maximum is then used to determine the rest-frame phase of the SN photometry to select the corresponding Hsiao et al. (2007) template spectrum to be used for K-corrections. In practice, the reddening is unknown before K-correction. The template is mangled using a smooth function to match the observed $B - V$ color when determining the B-band K-corrections, and $V - i'/I/R$ when determining the V-band K-corrections to minimize extrapolation errors. The smooth function used to mangle the template spectra is the Fitzpatrick & Massa (1999) reddening law assuming $R_V = 3.1$. The K-corrections are then measured by the difference in the synthetic magnitudes of the mangled spectrum at a redshift of zero and the given redshift of the SN (shown as red data points in Figure 2). The filter-vague FPCA decomposition of He et al. (2018) shows that the light curves of SNe Ia can be decomposed into a single set of FPCA vectors independent of the filter bands employed. This implies that the K-correction itself can also be decomposed into the same FPCA basis. The measured K-correction magnitudes at different epochs are further fitted using the He et al. (2018) FPCA templates with the mean component taken out and the maximum epoch fixed by the previous FPCA fit using `pycmpfit` χ^2 minimization. The final adopted values of the K-corrections (black cross in Figure 2) and their corresponding errors (shaded region in Figure 2) at desired epochs are then calculated from the fitted curve.

2.5. Host Reddening

Extinction can only make objects redder. Assuming that the intrinsic colors of SNe Ia are uniquely determined by the light-curve width as measured by the $\Delta m_{15}(B)$ values, one can expect there to be a "blue edge" in the distribution of the observed colors when the observed colors are plotted together with the $\Delta m_{15}(B)$ (Figure 3). With a large sample of SNe Ia, we may assume this blue edge to represent the intrinsic colors of SNe Ia for a given $\Delta m_{15}(B)$, and the reddening due to dust in the host-galaxy $E(B - V)_{\rm host}$ can be deduced by the difference between the observed colors and this ridge line. Figure 3 shows the MW- and K-corrected $B_{\rm max} - V_{\rm max}$ versus $\Delta m_{15}(B)$. We estimate the position of the "blue edge" by fitting a second-order polynomial ($B_{\rm max} - V_{\rm max} = A \times (\Delta m_{15}(B) - 1.1)^2 + C$, where A and C are parameters) to the ridge line that divides the SN sample into two groups, with the bluer group having 10% of the total number of the SNe in the sample. To do so robustly, 500 bootstrapped samples are generated with replacements from the data set, leading to 500 estimates of the blue ridge lines. The median and standard deviation of these 500 ridge lines are used as the line of the intrinsic color and its corresponding uncertainties, respectively. Uncertainties of the host-galaxy extinction are then estimated by the quadrature sum of uncertainties in $B_{\rm max} - V_{\rm max}$ and the uncertainties of the lower boundaries of the intrinsic colors. The equation for the final ridge line is

$$(B_{\rm max} - V_{\rm max})({\rm mag}) = 0.188 \times (\Delta m_{15}(B)({\rm mag}) - 1.1)^2 - 0.021.$$

3. Spectra

Spectra of our 91T/99aa-like sample are plotted in Figure 4 at different epochs relative to the B-band maximum. For SN

[15] https://github.com/cosmonaut/pycmpfit

Table 7
Parameters of 91T/99aa-like SNe Ia in Our Sample

SN (subtype[a])	z_{CMB}	$pEW_{nearmax}$(Si II λ6355) (Å)	$E(B-V)_{host}$	Hubble Residual (mag)	$t_{max}(B)$ (MJD)	$\Delta m_{15}(B)$ (mag)	$m_{max}(B)$ (mag)	SN (subtype[a])	PC1 (B)	PC2 (B)	$t_{max}(V)$ (MJD)	$\Delta m_{15}(V)$ (mag)	$m_{max}(V)$ (mag)	PC1 (V)	PC2 (V)
LSQ 15aae	0.0518	⋯	0.27 (0.04)	−0.35 (0.31)	57116.45 (0.35)	0.88 (0.05)	17.77 (0.03)	LSQ 15aae	−0.28 (0.32)	−0.03 (0.20)	57118.78 (0.35)	0.58 (0.04)	17.51 (0.02)	−0.39 (0.24)	0.00 (0.12)
PS 15sv (3)	0.0333	32.0	0.05 (0.04)	−0.26 (0.33)	57114.35 (0.85)	1.07 (0.05)	16.31 (0.04)	PS 15sv (3)	1.25 (0.51)	−0.35 (0.21)	57115.85 (0.32)	0.69 (0.03)	16.28 (0.02)	0.52 (0.19)	0.04 (0.08)
SN 1991T (4)	0.0069	42.2	0.21 (0.02)	−2.00 (0.47)	48375.52 (0.18)	0.94 (0.01)	11.60 (0.01)	SN 1991T (4)	−0.13 (0.09)	−0.06 (0.04)	48378.19 (0.12)	0.62 (0.01)	11.41 (0.01)	−0.34 (0.07)	0.19 (0.04)
SN 1995bd (2)	0.0144	20.1	0.44 (0.04)	−0.38 (0.35)	50085.74 (0.21)	0.85 (0.05)	15.51 (0.03)	SN 1995bd (2)	−0.98 (0.31)	0.24 (0.13)	50087.50 (0.22)	0.69 (0.04)	15.08 (0.02)	−0.29 (0.23)	0.43 (0.11)
SN 1998ab (0)	0.0279	4.5	0.10 (0.05)	−0.37 (0.34)	50913.82 (0.16)	1.09 (0.04)	16.00 (0.03)	SN 1998ab (0)	1.48 (0.28)	−0.46 (0.09)	50915.94 (0.25)	0.62 (0.04)	15.92 (0.03)	0.12 (0.25)	−0.10 (0.11)
SN 1998es (5)	0.0096	53.0	0.14 (0.01)	−0.01 (0.35)	51142.20 (0.04)	0.71 (0.01)	13.87 (0.01)	SN 1998es (5)	−0.78 (0.08)	−0.67 (0.04)	51144.30 (0.05)	0.52 (0.01)	13.72 (0.01)	−0.76 (0.05)	−0.10 (0.03)
SN 1999aa (5)	0.0152	52.4	0.01 (0.01)	0.29 (0.32)	51231.73 (0.04)	0.73 (0.01)	14.76 (0.01)	SN 1999aa (5)	−0.55 (0.05)	−0.74 (0.03)	51233.92 (0.05)	0.54 (0.01)	14.74 (0.00)	−0.51 (0.04)	−0.12 (0.02)
SN 1999ac (8)	0.0098	80.4	0.06 (0.02)	0.01 (0.37)	51249.47 (0.03)	1.20 (0.01)	14.07 (0.01)	SN 1999ac (8)	1.09 (0.05)	0.20 (0.03)	51252.63 (0.07)	0.65 (0.01)	14.03 (0.00)	0.41 (0.04)	−0.12 (0.03)
SN 1999aw (4)	0.0392	48.7	0.12 (0.02)	−0.11 (0.29)	51253.93 (0.23)	0.68(0.01)	16.72 (0.01)	SN 1999aw (4)	−1.90 (0.11)	0.15 (0.04)	51255.63 (0.24)	0.57 (0.02)	16.59 (0.01)	−1.27 (0.10)	0.45 (0.07)

Note.
[a] Subtype classification based on the strength of pEW_{max}(Si II $\lambda\lambda$6355). The classification is the floor hexadecimal integer of pEW_{max}(Si II $\lambda\lambda$6355)/10 (see Section 5.3 for more details).
(This table is available in its entirety in machine-readable form.)

Table 8
Parameters of Normal SNe Ia in Our Sample

SN (subtype[a])	z_{CMB}	$pEW_{nearmax}$(Si II λ6355) (Å)	$E(B-V)_{host}$	Hubble Residual (mag)	$t_{max}(B)$ (MJD)	$\Delta m_{15}(B)$ (mag)	$m_{max}(B)$ (mag)	SN (subtype[a])	PC1 (B)	PC2 (B)	$t_{max}(V)$ (MJD)	$\Delta m_{15}(V)$ (mag)	$m_{max}(V)$ (mag)	PC1 (V)	PC2 (V)
SN 1998dh (C)	0.0078	121.6	0.12 (0.02)	0.09 (0.25)	51029.19 (0.03)	1.23 (0.01)	13.88 (0.00)	SN 1998dh (C)	2.01 (0.05)	−0.40 (0.03)	51031.57 (0.04)	0.69 (0.01)	13.77 (0.01)	0.90 (0.04)	−0.25 (0.02)
SN 1998dm (6)	0.0060	68.4	0.33 (0.02)	1.07 (0.32)	51060.38 (0.07)	0.87 (0.01)	14.68 (0.01)	SN 1998dm (6)	0.14 (0.10)	−0.61 (0.04)	51062.06 (0.05)	0.60 (0.01)	14.37 (0.01)	−0.08 (0.06)	−0.07 (0.02)
SN 1999cp (9)	0.0099	99.6	0.04 (0.02)	0.10 (0.25)	51363.46 (0.04)	0.99 (0.01)	13.93 (0.00)	SN 1999cp (9)	0.90 (0.06)	−0.60 (0.04)	51364.71 (0.05)	0.66 (0.01)	13.91 (0.00)	0.15 (0.05)	0.09 (0.03)
SN 1999dk (C)	0.0140	126.4	0.12 (0.02)	−0.15 (0.18)	51414.78 (0.13)	1.09 (0.02)	14.79 (0.01)	SN 1999dk (C)	1.48 (0.16)	−0.54 (0.09)	51416.88 (0.15)	0.68 (0.02)	14.69 (0.01)	0.63 (0.13)	−0.13 (0.06)
SN 2000cn (B)	0.0227	118.6	0.17 (0.02)	−0.05 (0.12)	51707.17 (0.04)	1.63 (0.02)	16.53 (0.01)	SN 2000cn (B)	4.78 (0.23)	−0.62 (0.15)	51709.58 (0.08)	0.96 (0.01)	16.33 (0.01)	3.79 (0.22)	−0.61 (0.11)
SN 2000cw (B)	0.0288	111.4	0.11 (0.02)	0.11 (0.12)	51748.18 (0.19)	1.18 (0.03)	16.66 (0.01)	SN 2000cw (B)	2.31 (0.46)	−0.64 (0.34)	51751.05 (0.22)	0.69 (0.02)	16.57 (0.01)	1.23 (0.34)	−0.45 (0.19)
SN 2000dk (C)	0.0160	121.6	−0.01 (0.02)	0.05 (0.15)	51812.27 (0.06)	1.64 (0.02)	15.30 (0.01)	SN 2000dk (C)	4.29 (0.15)	−0.22 (0.09)	51814.42 (0.06)	0.95 (0.01)	15.28 (0.01)	3.33 (0.09)	−0.44 (0.06)
SN 2000dn (9)	0.0307	98.7	0.08 (0.04)	0.06 (0.15)	51824.74 (0.14)	1.06 (0.04)	16.55 (0.02)	SN 2000dn (9)	1.32 (0.36)	−0.47 (0.25)	51827.22 (0.17)	0.69 (0.03)	16.49 (0.02)	0.94 (0.24)	−0.23 (0.14)
SN 2000dr (C)	0.0180	124.9	0.08 (0.03)	−0.04 (0.16)	51834.31 (0.09)	1.84 (0.03)	15.94 (0.01)	SN 2000dr(C)	5.00 (0.00)	0.27 (0.16)	51836.42 (0.14)	1.00 (0.02)	15.77 (0.01)	3.52 (0.19)	−0.32 (0.12)
SN 2000fa (9)	0.0215	90.9	0.19 (0.02)	−0.05 (0.13)	51891.96 (0.14)	0.89 (0.02)	15.91 (0.01)	SN 2000fa (9)	0.30 (0.13)	−0.59 (0.07)	51893.77 (0.22)	0.60 (0.01)	15.73 (0.01)	−0.03 (0.09)	−0.13 (0.05)

Note.
[a] Subtype classification based on the strength of pEW_{max}(Si II $\lambda\lambda$6355). The classification is the floor hexadecimal integer of pEW_{max}(Si II $\lambda\lambda$6355)/10 (see Section 5.3 for more details).
(This table is available in its entirety in machine-readable form.)

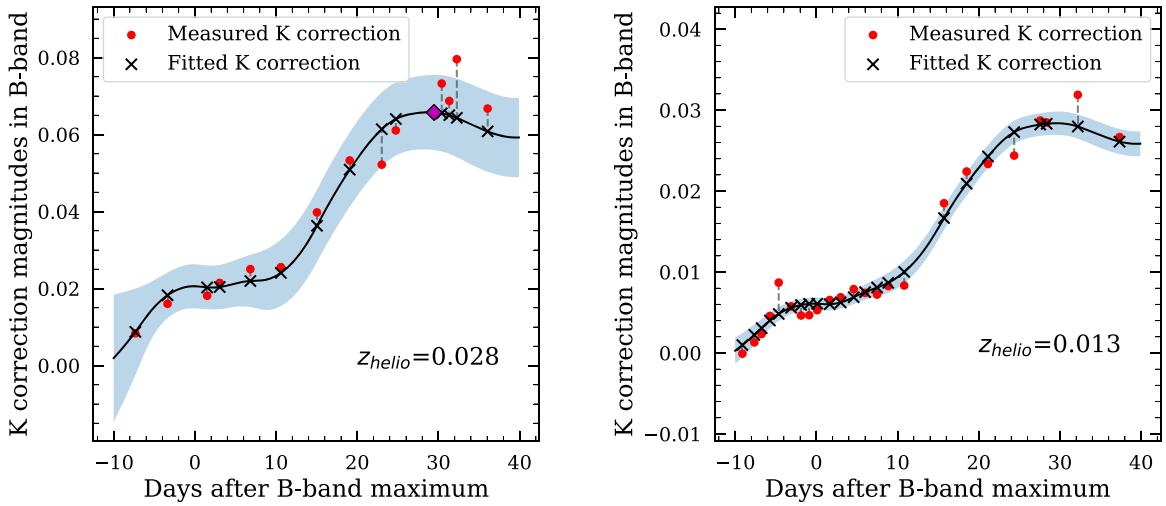

Figure 2. Examples of K-correction calculation for SN 2016gcl (left) and SN 2019vrq (right). The red data points are the K-correction values measured from the mangled Hsiao template. The black line is the FPCA fit to the red data points. The shaded region is the error of the FPCA fit. And the black crosses are the adopted K-correction values derived from the fitted FPCA curve. By fitting a smooth curve to the measured K-correction, we cannot only get the error estimates but also the K-correction values of the epochs when colors to which the spectra need to be mangled to match are not available (one example is the purple diamond on the left panel).

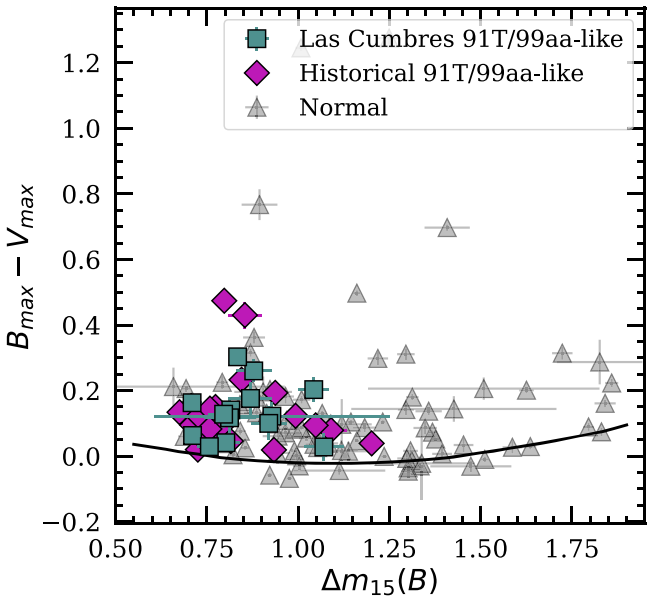

Figure 3. Observed $B_{\max} - V_{\max}$ (MW extinction and K-corrected) vs. $\Delta m_{15}(B)$. Extinction can only cause $B_{\max} - V_{\max}$ to increase in value, thus the lower envelope (plotted as a black solid line) can be used as an extinction-free curve to correct for host extinction (Section 2.5). 91T/99aa-like data points are plotted in green squares, and historical 91T/99aa-like data points are plotted in purple diamonds. Normal SNe Ia are plotted in gray triangles.

2018apo we do not have *B*-band photometry, so the maximum date was determined using *g*-band photometry. These spectra were collected from the Open Supernova Catalogue (Guillochon et al. 2017). The spectra are grouped into five groups each showing the data within 2 days of (a) −13 days, (b) −8 days, (c) −4 days, (d) 0 days, and (e) +6 days from *B*-band maximum for our 91T/99aa-like sample. The strength of the Si II 6355 ± 5 Å around maximum increases from top to bottom for each group. Spectra of SN 1991T, SN 1999aa, and the spectroscopically normal SN 2004eo at the relevant phases are plotted in bold lines together with each group for comparison.

Not all 91T/99aa-like events classified by their spectra are slow decliners. The 91T/99aa-like objects with $\Delta m_{15}(B) > 1.0$ mag are plotted in red in Figure 4. It is readily seen that some of the SNe with the shallowest Si II$\lambda\lambda$6355 lines are actually not slow decliners. The slowest decliners among 91T/99aa-like objects with $\Delta m_{15}(B) < 0.8$ mag are plotted in a dashed gray line. Although still showing shallower Si II lines, the spectra of 91T/99aa-like objects show all the major spectral features of normal SNe Ia at about 6 days after maximum. This suggests strongly that they share similar ejecta structures with spectroscopically normal SNe Ia and are likely to originate from similar physical systems and processes.

3.1. Pseudo-equivalent Widths

The true continuum in an SN Ia spectrum cannot be formally determined, but the strength of an absorption line can be measured with respect to the flux at wavelengths shorter and longer than that of a given line. This is called the pseudo-equivalent width (pEW). It is defined as follows:

$$\mathrm{pEW} = \sum_{i=1}^{N}\left(1 - \frac{f(\lambda_i)}{f_c(\lambda_i)}\right), \quad (4)$$

where λ_1 and λ_N define the boundaries between which the pEW is calculated, $f(\lambda_i)$ is the spectral flux at wavelength λ_i, and $f_c(\lambda_i)$ is the pseudo-continuum flux level defined by the line connecting the endpoints at λ_1 and λ_N.

To measure the pEW of the Si II$\lambda\lambda$6355 line, the endpoints are found by selecting the point with the maximum flux of binned spectra (with a bin size of 40 Å) in the wavelength ranges [5820 Å, 6000 Å] and [6200 Å, 6540 Å] for the red side and blue side, respectively. The endpoints are further inspected by eye. We use a Monte Carlo method to calculate the errors of the pEW measurements. First we find the signal-to-noise ratio at each wavelength by dividing the original spectrum with a heavily smoothed spectrum (smoothed by the wavelet transformation method described by Wagers et al. 2010). Then the standard deviation of the signal-to-noise ratio at each pixel is found by the standard deviation of signal-to-noise ratios

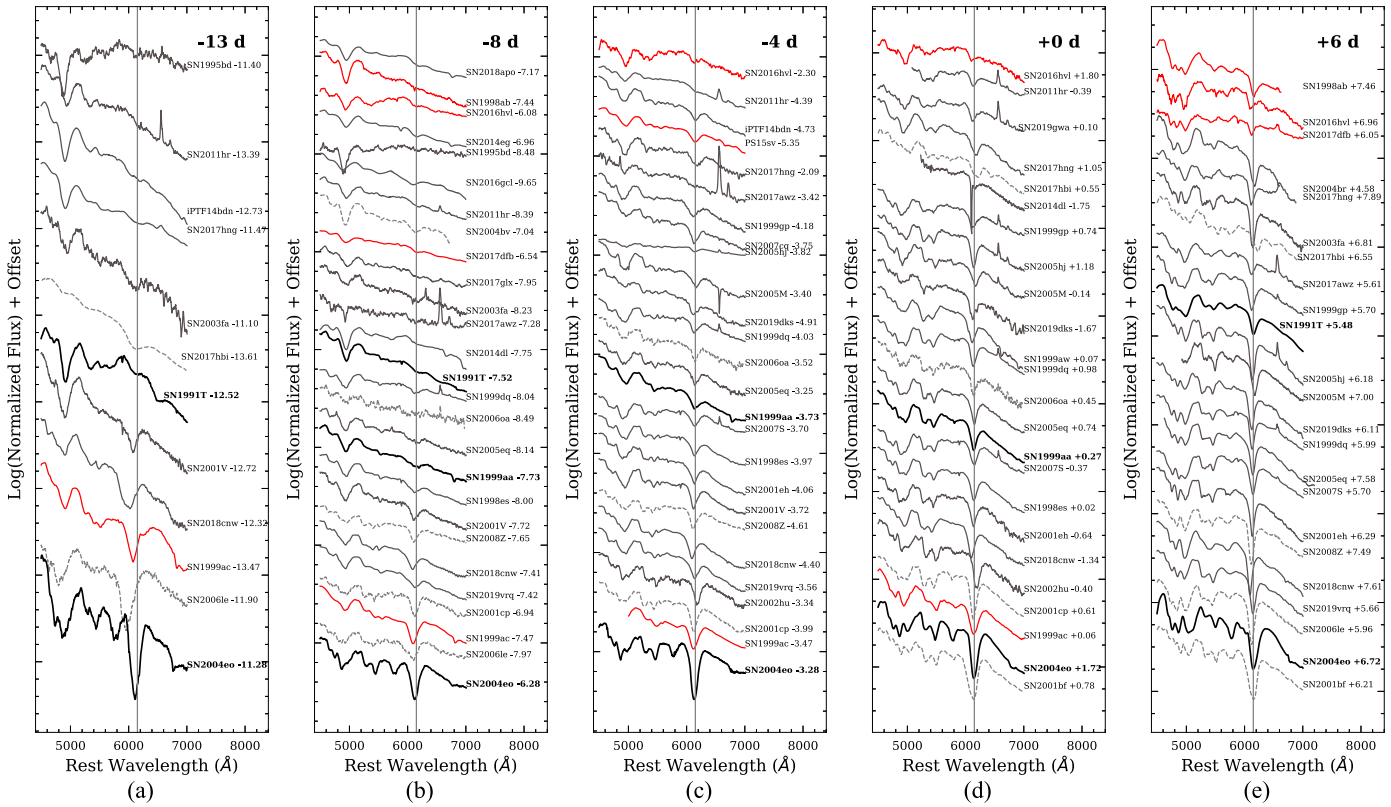

Figure 4. Spectra within 2 days of (a) −13 days, (b) −8 days, (c) −4 days, (d) 0 days, and (e) +6 days of our 91T/99aa-like sample. The Si II 6355 ± 5 Å around maximum increases from top to bottom for each panel. SN 1991T, SN 1999aa, and the typical normal Type Ia SN 2004eo are plotted in bold. 91T/99aa-like objects with $\Delta m_{15}(B) > 1.0$ mag are plotted in red. And normal objects in our sample with $\Delta m_{15}(B) < 0.8$ mag are also plotted in dashed gray lines. A vertical gray line at 6150 Å is also plotted to guide the eye.

within 50 Å. Next, we create a large number of simulated spectra with random noise generated using a Gaussian distribution with this calculated standard deviation. Finally, the pEW measurement is obtained for each of the simulated spectra, and the mean and the standard deviation of these pEW measurements give our final pEW value and its corresponding 1σ error.

4. Standardization

The discovery of the accelerating expansion of the universe using SNe Ia was based on the discovery of the relationship between the SN Ia peak luminosity magnitude and the light-curve decline rate (Phillips 1993) and the peak luminosity magnitude and color relationship found later (Hamuy et al. 1996a; Tripp 1998), which make SNe Ia standardizable candles. 91T/99aa-like SNe Ia are inevitably overrepresented in flux-limited surveys. Understanding the intrinsic properties of these SNe is therefore crucial to controlling the systematic errors when using SNe Ia to measure distances.

A Hubble diagram using SNe Ia can be used to constrain the cosmological acceleration parameters, but it requires a high-redshift SNe Ia sample to be able to differentiate between different cosmology models (Goobar & Perlmutter 1995). However, a nearby SN Ia sample is also necessary to evaluate the precision of SNe Ia as standardizable candles, specifically, the standardizability of 91T/99aa-like objects in our case.

In this section, we evaluate the precision to which 91T/99aa-like SNe Ia may be used as standardizable candles. Recently, more sophisticated modeling and parameterization of SNe Ia are used for SN Ia standardization, for example SALT2 (Guy et al. 2007, 2010; Betoule et al. 2014), SNEMO (Saunders et al. 2018), and SUGAR (Léget et al. 2020). Here we adopt the simple two-parameter parameterization using the decline rate $\Delta m_{15}(B)$ and host-color excess $E(B-V)_{\rm host}$ for standardization:

$$m_B^* = m_B(0)^* + b[\Delta m_{15}(B) - 1.1] + R_B E(B-V)_{\rm host}\ , \quad (5)$$

where $m_B^* = m_B - R_B E(B-V)_{\rm gal} - K_B$ is the MW and K-corrected apparent peak magnitudes of SNe Ia in the B band, $m_B(0)^*$ is the expected apparent peak magnitude of our fiducial SN Ia at redshift z, with $\Delta m_{15}(B) = 1.1$ and $E(B-V) = 0$. Here we adopt the approximation of $m_B(0)^* = 5log_{10}(cz) + k$ as all SNe in our sample have $z \lesssim 0.1$. Thus, we immediately have $H_0 = 10^{0.2(M_B(0)+k+25)}$, where $M_B(0)$ is the absolute peak magnitude of a fiducial SN Ia. The global parameters are then (b, R_B, k), where k is the intercept of the Hubble diagram. The Phillips luminosity–decline relationship (Phillips 1993) is represented by the parameter b, the luminosity–color relationship is determined by R_B, and k contains the information of the Hubble constant at present, or equivalently, the absolute magnitude of the fiducial SN Ia.

In the analyses presented here, heliocentric redshifts were converted into the CMB frame using the velocity vector determined by Lineweaver (1997) to calculate luminosity distances. The uncertainty in the redshifts due to peculiar velocities is assumed to be $\sigma_z = 0.001$ (300 km s^{-1} in velocity).

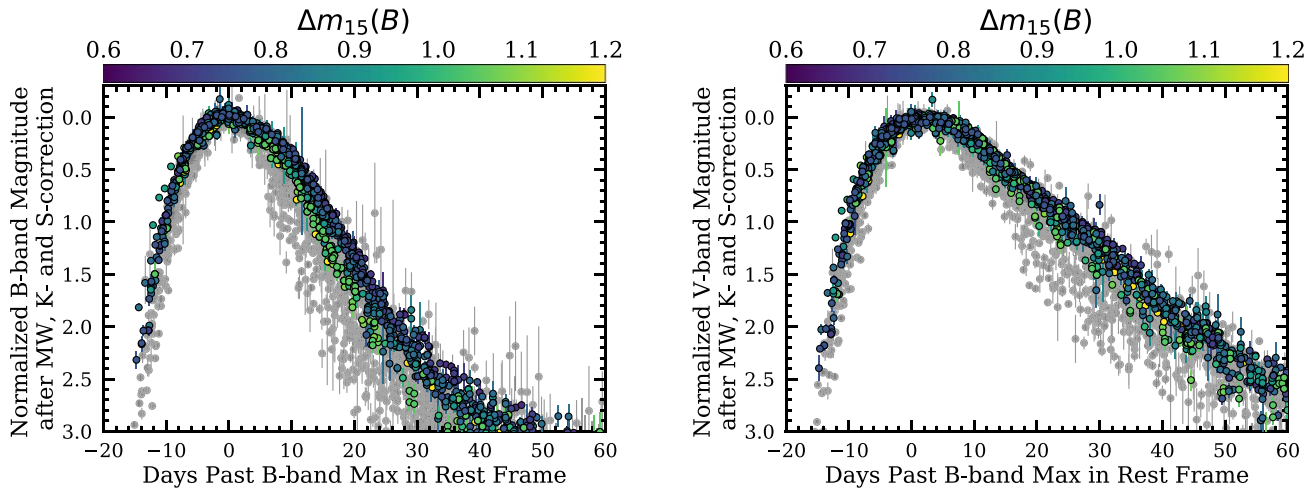

Figure 5. *B*- and *V*-band light curves for the SNe used in this paper. The light curves have been shifted vertically for better visualization. The gray data points are normal SNe Ia, while the data points of 91T/99aa-like SNe Ia are color-coded by $\Delta m_{15}(B)$.

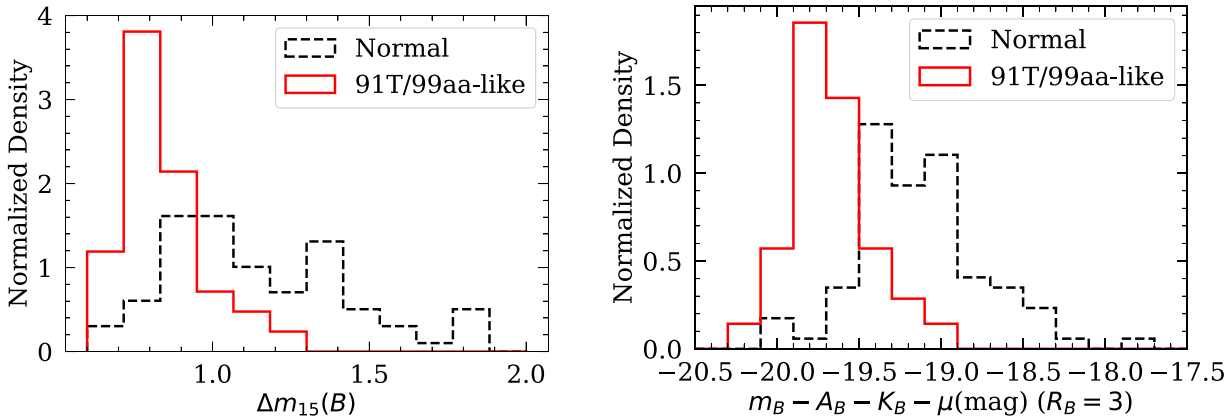

Figure 6. Left: histogram of Δm_{15} in the *B* band. Right: histogram of absolute magnitudes at maximum in the *B* band assuming a constant $R_B = 3$.

Parameters in Equation (5) are determined by fitting SNe in our sample with $z_{\rm cmb} > 0.01$ using a χ^2 minimization of

$$\chi^2 = \sum_{i=1}^{N} \frac{(m^*_{B\rm corr} - m_B(0)^*)^2}{\sigma^2_{m^*_{B\rm corr},i} + \sigma^2_{\rm intrinsic} + \sigma^2_{\rm pec}}, \quad (6)$$

where $m^*_{B\rm corr} = m^*_B - b\Delta(m_{15}(B) - 1.1) - R_B E(B-V)$, $\sigma_{\rm pec}$ accounts for peculiar velocity ($v_{\rm pec} = 300\,{\rm km\,s^{-1}}$),

$$\sigma^2_{m^*_{Bcorr}} = \sigma^2_{m^*_B} + b^2\sigma^2_{\Delta m_{15}(B)} + R_B^2\sigma^2_{E(B-V)}, \quad (7)$$

and $\sigma^2_{\rm intrinsic}$ accounts for possible intrinsic scatter in SNe Ia, which is determined so that the final $\chi^2_\nu = 1$.

5. Results

5.1. Photometric Properties of 91T/99aa-like SNe Ia

The *B*- and *V*-band light curves of the SNe used in this analysis are plotted together in Figure 5. Gray points are for normal SNe Ia while 91T/99aa-like objects are color-coded by the value of $\Delta m_{15}(B)$. As expected, light curves of 91T/99aa-like SNe are typically broader compared to those of normal SNe Ia. This trend is more pronounced in the *V* band.

Host-galaxy extinction needs to be taken out if one wants to compare the intrinsic brightness of 91T/99aa-like SNe to normal SNe Ia. The extinction is commonly characterized by the total-to-selective extinction ratio $R_V = A_V/E(B-V)$, where $E(B-V) = A_B - A_V$. Previous studies of the host extinction from SNe Ia yielded diverse values of R_V ranging from $R_V = 1$ to $R_V = 3.5$ (e.g., Tripp 1998; Phillips et al. 1999; Conley et al. 2007; Hicken et al. 2009; Wang et al. 2009). For a rough comparison of the intrinsic luminosity distributions between 91T/99aa-like SNe and normal SNe Ia without any standardization, we take a moderate value of $R_{V(\rm host)} = 2$ with $E(B-V)_{\rm host}$ calculated from Section 2.5. In Figure 6 we plot the distribution of the decline rate parameter $\Delta m_{15}(B)$, and the extinction- and K-corrected absolute *B*-band magnitudes when assuming host $R_V = 2$ for all 123 SNe Ia included in this work (SN 2018apo is not included in this figure as we do not have SN 2018apo *B*-band data.). The distance moduli are calculated using the aforementioned assumed cosmology.[16] The weighted mean and standard deviation of the full sample's absolute peak *B*-band magnitude and $\Delta m_{15}(B)$ are listed in Table 9.

The spectroscopically peculiar 91T/99aa-like objects are $\sim$0.4 mag brighter than normal SNe Ia after applying K-corrections and correcting for MW extinction and host-galaxy extinction. Moreover, these overluminous events seem to have a more uniform peak luminosity and a more uniform distribution of values of the decline rate parameter $\Delta m_{15}(B)$,

[16] Since our SNe are nearby ($z < 0.1$), luminosity distances are effectively independent of any sensible combination of Ω_M and Ω_Λ.

Table 9
Weighted Means and Standard Deviations of Absolute Peak Magnitudes and $\Delta m_{15}(B)$ in Figure 6

SN subclass	N_{SN}	$\overline{M_B}$	σ_{M_B}	$\overline{\Delta m_{15}(B)}$	$\sigma_{\Delta m_{15}(B)}$
Normal	87	−19.30	0.47	1.09	0.32
91T/99aa-like	36	−19.70	0.32	0.82	0.13

with a standard deviation of about 0.13 mag compared to 0.32 mag for normal SN Ia.

5.2. The Hubble Diagram

We standardize our sample using the method described in Section 4 in two cases: For one, we assume 91T/99aa-like and normal SNe Ia share the same intrinsic scatter $\sigma_{\rm int}$, and for the other we assume each group has a different intrinsic scatters $\sigma_{\rm int}$(91T/99aa -like) and $\sigma_{\rm int}$(normal) (so that for each group, $\chi^2_\nu \approx 1$ after fitting). The final fitting parameters for both cases are summarized in Table 10. And the Hubble residuals for the case with different intrinsic scatters are listed in Tables 7 and 8. Below we focus on the case with different intrinsic scatters.

In Figure 7, we present the *B*-band residual Hubble diagram and the histogram of Hubble residuals along with the fitted Gaussian ideogram.[17] The weighted mean Hubble residual for normal SNe Ia and 91T/99aa-like SNe Ia with $z_{\rm cmb} > 0.01$ are 0.03 mag and −0.19 mag, respectively, and the peaks in the Gaussian ideogram for normal SNe Ia and all 91T/99aa-like SNe Ia in our sample are 0.01 mag and −0.17 mag, respectively, suggesting that even fully corrected, 91T/99aa-like SNe Ia still are ∼0.2 mag brighter than normal SNe Ia (Boone et al. 2021; Reindl et al. 2005).[18] Therefore, careful classification of 91T/99aa-like SNe is needed to avoid possible pollution of the cosmological sample of SNe Ia or to introduce an additional parameter to account for the Hubble residual offset in 91T/99aa-like and normal SNe.

The intrinsic scatter for 91T/99aa-like is $\sigma_{\rm int}$(91T/99aa − like) = 0.28 mag, more than that of normal SNe Ia ($\sigma_{\rm int}$(normal) = 0.05 mag). The weighted rms (wrms) are 0.25 ± 0.03 mag and 0.14 ± 0.02 mag for 91T/99aa-like and normal SNe Ia, respectively. It suggests that 91T/99aa-like SNe are also excellent relative distance indicators, though not as precise as normal SNe Ia, and can be used to delineate the Hubble flow to a precision of 12%. However, an additional parameter needs to be introduced to bring 91T/99aa-like SNe to the same standard value as normal SNe Ia. Note that for absolute distance determination, it requires independent estimates of nearby SN hosts (e.g., Riess et al. 2019), which is beyond the scope of this paper.

[17] See https://pdg.lbl.gov/2015/reviews/rpp2015-rev-rpp-intro.pdf for more discussion on the ideogram.

[18] A similar conclusion about the over-luminosity of 91T/99aa-like SNe has been drawn by M. M. Phillips (Phillips et al. 2022, submitted) based on data from the Carnegie Supernova Project.

5.3. Si II λλ6355 pEW

We used pEW measurements of the Si II λλ6355 line from the spectra in our database that are closest to—and within 10 days from—the *B*-band maximum as our Si IIλλ6355 pEW measurement around maximum. In total, we have such measurements of 79 normal SNe Ia and 35 91T/99aa-like SNe. Final pEW measurements are listed in Tables 7 and 8. Hubble residuals versus $\rm pEW_{max}$(Si II λλ6355) are plotted in Figure 10 (See also M. M. Phillips 2023 for further discussion). As $\rm pEW_{max}$(Si II λλ6355) increases from 0 Å to 150 Å, Hubble residuals increase first and then stay nearly constant. Thus, we fit a continuous broken line so that Hubble residual linearly increases with $\rm pEW_{max}$(Si II λλ6355) first, and stays constant beyond a $\rm pEW_{max}$(Si II λλ6355) value. The line is fitted using χ^2 minimization (see Section 15.3 in Press et al. 2007) with `pycmpfit`. The best-fit result is

$$\text{Hubble residual (mag)} = \begin{cases} (0.009 \pm 0.003) \times \text{pEW(Si II } \lambda\lambda 6355)(\text{Å}) - (0.482 \pm 0.154), & \text{pEW(Si II } \lambda\lambda 6355) < 55.62 \text{ Å} \\ 0.036, & \text{otherwise.} \end{cases} \quad (8)$$

There does not seem to be a correlation between the Hubble residual and $\Delta m_{15}(B)$ as shown in the left panel in Figure 9. Thus, the broken linear correlation between the Hubble residual and Si II λλ6355 is unlikely due to the artifacts of standardizations. As shown in the right panel of Figure 9, the relation between $\Delta m_{15}(B)$ and $\rm pEW_{max}$ (Si II λλ6355) is nonlinear. Thus, a linear correlation of $\Delta m_{15}(B)$ to the Hubble residual cannot fully take out the dependency of the Hubble residual on $\rm pEW_{max}$(Si II λλ6355).

For our sample of 113 objects with pEW(Si II λλ6355) near maximum and *B*-band light-curve data, after taking out the fitted linear relationship between $\rm pEW_{max}$(Si II λλ6355) and the light-curve shape- and color-corrected Hubble residual, the wrms of the Hubble residuals of the 113 objects decreases from 0.17 mag to 0.14 mag (for 34 91T/99aa-like objects, wrms decreases from 0.26 mag to 0.22 mag, and for 79 normal objects, wrms decreases from 0.129 mag to 0.125 mag).

The Hubble residual offset in 91T/99aa-like and normal SNe Ia can then be explained by the positive linear correlation in between the Hubble residual and the pEW, as most SNe Ia have $\rm pEW_{max}$(Si II λλ6355) < 55.6 Å, and 91T/99aa-like SNe are characterized by shallow Si II lines.

We suggest a new subtype classification scheme for SNe Ia as follows. The SNe Ia is subdivided using a hexadecimal number, with 0 being the extreme SN 1991T–like showing undetectable Si II λλ6355 line, and F being the extreme case with $\rm pEW_{max}$(Si II λλ6355) beyond 160 Å. In between these extreme cases, the subtypes are given by a hexadecimal number that is the integer part of $pEW_{\rm max}$(Si II λλ6355)/10. The subtypes of SNe in our sample are given in Tables 7 and 8.

In the right panel of Figure 9 we plot the $pEW_{\rm max}$(Si II λλ6355) vs $\Delta m_{15}(B)$. As can be seen from the figure, $\Delta m_{15}(B)$ does not always increase as $pEW_{\rm max}$(Si II λλ6355) increases. There are a few objects with normal decline rates yet have very shallow Si II lines, and objects with slow decline rates but moderate strength of Si II lines. To show that the effect is not some artifact from fitting, the light curves of normal objects with $\Delta m_{15}(B) < 0.8$ mag and 91T/99aa-like objects with

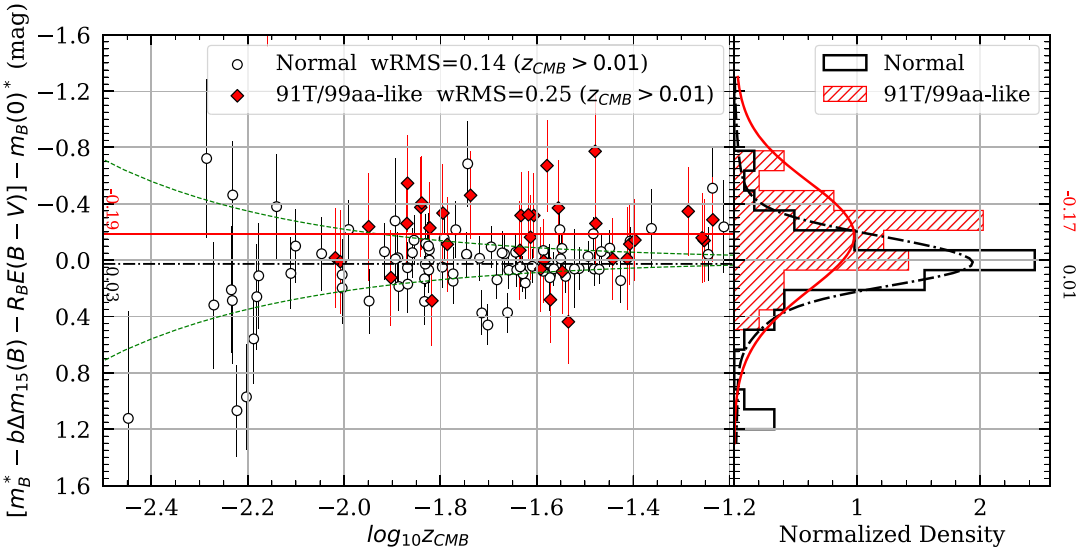

Figure 7. Hubble diagram residual (left) and residual histogram (right) in B band for 36 91T/99aa-like SNe Ia (in filled circles) and 87 normal SNe Ia (in open circles) when assuming these two groups have different intrinsic scatters (0.28 mag for 91T/99aa-like, and 0.05 mag for normal SNe Ia). Left: the weighted mean Hubble residuals for 91T-like SNe Ia and normal SNe Ia are 0.03 mag and −0.18 mag, which are also plotted as horizontal lines on the plot (solid line for 91T-like SNe, dashed–dotted line for normal SNe Ia). The dashed line denotes the peculiar velocity effect with $v_{pec} = 300$ km s^{-1}. Right: Distribution of Hubble residuals. The Gaussian ideograms of each group are also plotted (solid line for 91T/99aa-like, dashed–dotted line for normal SNe Ia). The peak of resulting Gaussian ideograms are 0.01 mag and −0.17 mag for normal SNe Ia and 91T/99aa-like SNe Ia, respectively.

Table 10
Fitting Parameters of Hubble Diagram

Condition on σ_{int}	b	R_B	k	σ_{int} (mag)		rms ($z_{cmb} > 0.01$) (mag)		wrms ($z_{cmb} > 0.01$) (mag)	
				normal	91T/99aa-like	normal	91T/99aa-like	normal	91T/99aa-like
$\sigma_{int(normal)} = \sigma_{int(91T/99aa)}$	0.88 ± 0.06	3.13 ± 0.17	-3.58 ± 0.03	0.14	0.14	0.18 ± 0.03	0.25 ± 0.03	0.16 ± 0.02	0.24 ± 0.03
$\sigma_{int(normal)} \neq \sigma_{int(91T/99aa)}$	0.81 ± 0.05	3.35 ± 0.15	-3.57 ± 0.02	0.05	0.28	0.17 ± 0.02	0.26 ± 0.03	0.14 ± 0.02	0.25 ± 0.03

$\Delta m_{15}(B) > 1.0$ mag are shown in Figure 8, and their spectra are highlighted in Figure 4.

6. Discussion and Conclusions

Spectroscopically confirmed peculiar SNe Ia such as overluminous 91T/99aa-like SNe Ia have generally been excluded from cosmological use of SNe Ia. However, those overluminous events will be overrepresented in future flux-limited surveys. Furthermore, the spectral evolution of 91T/99aa-like objects resembles that of normal SNe Ia after maximum light, which makes keeping the homogeneity of the SN Ia cosmological sample more difficult. Hence, it is crucial to understand the intrinsic properties of these overluminous SNe Ia to avoid inevitable systematic errors in luminosity distances.

To address this problem, we obtained multiepoch optical $BVg'r'i'$ photometric observations of 16 91T/99aa-like SNe Ia taken by Las Cumbres Observatory in the redshift range $z = 0.011$ –0.057. This sample was analyzed together with 21 well-sampled photometric observations of 91T/99aa-like SNe Ia as well as 87 photometrically well-sampled normal SNe Ia from the literature. Our main conclusions are as follows:

1. When assuming host $R_V = 2$, after correcting for K-correction, MW extinction, and host extinction, the spectroscopically peculiar 91T/99aa-like objects are ∼0.4 mag brighter than the normal SNe Ia.
2. After being fully corrected (see Section 4), 91T/99aa-like objects are still ∼0.2 mag brighter than normal SNe Ia.
3. 91T/99aa-like objects themselves are excellent relative distance indicators and can be used to delineate galaxies in the Hubble flow to 12% in distance.
4. $\Delta m_{15}(B)$ does not always increase as pEW_{max}(Si II $\lambda\lambda$6355) increases. For pEW_{max}(Si II $\lambda\lambda$6355) < 55.6 Å, light curves tend to decline faster with shallower Si II $\lambda\lambda$6355.
5. After being fully corrected, the Hubble residual still has a fairly strong linear correlation with pEW_{max}(Si II $\lambda\lambda$6355) for pEW_{max}(Si II $\lambda\lambda$6355) < 55.6 Å while the Hubble residual does not correlate with $\Delta m_{15}(B)$. This is due to the nonlinear relation between $\Delta m_{15}(B)$ and pEW_{max}(Si II $\lambda\lambda$6355). So a linear correction of $\Delta m_{15}(B)$ cannot fully take out the dependence of the Hubble residual on pEW_{max}(Si II $\lambda\lambda$6355), if any.

The current study is based on the optical data. In the NIR, the systematic offset of the Hubble residuals between 91T/99aa-like and normal SNe may be different from the optical. A careful analysis of the NIR properties of 91T/99aa-like SNe is needed.

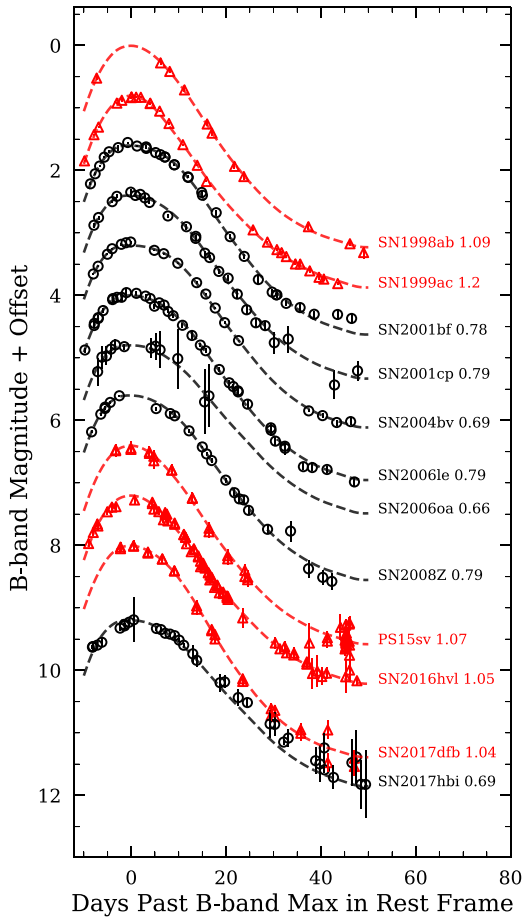

Figure 8. *B*-band light curves and fits of normal SNe Ia (in black circles) with $\Delta m_{15}(B) < 0.8$ mag and 91T/99aa-like SNe (in red triangles) with $\Delta m_{15}(B) > 1.0$ mag. $\Delta m_{15}(B)$ values are labeled next to each light curve.

The spectral evolution of 91T/99aa-like SNe Ia argues that early spectral data are needed for their identification. This may cause the SN Ia samples to be contaminated by misidentifications of 91T/99aa-like SNe if spectral data before optical maximum are missing. This would lead to large systematic biases in cosmological analyses if the fraction of 91T/99aa-like SNe Ia changes with redshift. High-mass but passive hosts are observed to produce SNe Ia over the full range of decline rates, whereas low-mass, star-forming hosts (which increase with redshift; Noeske et al. 2007; Daddi et al. 2007; Elbaz et al. 2007) preferentially give rise to slower-declining events like 91T/99aa-like SNe (Sullivan et al. 2010; Uddin et al. 2020). The fractional evolution of 91T/99aa-like SNe Ia will cause systematic errors of the SNe Ia Hubble residual to be as large as 0.2 mag in the extreme case at high redshifts where SNe Ia are dominated by 91T/99aa-like events. This will be very important on upcoming surveys like LSST/Rubin and WFIRST/Roman for which the projected uncertainties are smaller than the effects reported here.

Based on the postmaximum spectral similarities between 91T/99aa-like SNe Ia and the normal SNe Ia, it may be concluded that the 91T/99aa-like SNe Ia and normal SNe Ia could easily be confused with just photometric data. It is critical to identify them in future SN surveys, which aim at a much higher precision than today in cosmological applications. The 0.2 mag correction between 91T/99aa-like SNe and normal SNe Ia also depends on the relative abundances of 91T/99aa-like objects at different $pEW_{\rm max}$(Si II $\lambda\lambda$6355) since 91T/99aa-like objects with lower $pEW_{\rm max}$(Si II $\lambda\lambda$6355) have brighter Hubble residuals. Therefore, it will be necessary to construct a classification scheme of the 91T/99aa-like SNe. The correlation between the Hubble residual and pEW of the Si II $\lambda\lambda$6355 line seen in Figure 10 suggests that the strength of the Si II $\lambda\lambda$6355 line can be employed to subclassify SNe Ia. Instead of classifying SNe Ia with descriptive monikers such as 91T/99aa-like or shallow silicon, we suggest dividing the SN Ia types into subclasses based on the values of $pEW_{\rm max}$(Si II $\lambda\lambda$6355). The measured pEW values are typically in the range from 0 to 160 (see Figure 10); a single hexadecimal digit can be used to group them in intervals of 10, with the last class being inclusive of all SNe with $pEW_{\rm max}$(Si II $\lambda\lambda$6355) larger than 160 Å. The subclassification is natural as the presence of Si II is the basis for SN Ia classification. As the Si II line changes rapidly around maximum light, in the case where it is not easy to obtain spectra around maximum light, we recommend using the data-driven spectral modeling code introduced in Hu et al. (2022), which is able to model the spectrum at maximum well, given the observed spectra at other phases.

Another systematic effect that has been routinely addressed recently in cosmological samples is a ∼0.06 mag correction found from the empirical correlation between SN Ia–corrected Hubble residuals with the host-galaxy mass (the mass step; Kelly et al. 2010; Sullivan et al. 2010; Lampeitl et al. 2010; Gupta et al. 2011; Childress et al. 2013; Johansson et al. 2013). SNe Ia in high-mass, passive hosts appear to be brighter than those in low-mass, star-forming hosts. It can be easily seen that 91T/99aa-like SNe Ia have a host mass step that is in the opposite direction since they are associated with active star formation (Hakobyan et al. 2020). Thus, the fraction of 91T/99aa-like SNe Ia will affect the size of the mass step. These effects need to be carefully taken into account for future surveys to measure cosmological parameters with better control of systematics for future surveys. Our study suggests further that shallow Si II line SNe Ia cannot be the source of the mass step effect, and that the mass step is caused by SNe Ia with normal Si II line strength. However, for SNe at high redshifts, the fractional contribution of 91T/99aa-like events may become larger, which will lead to a systematic effect that must be taken into account for precision cosmology measurements.

The correlation between the luminosity and the pEW of the Si II 6355 line may also suggest that the group of 91T/99aa-like events consists of SNe with related physical origins. One such possibility is that they are similar events that differ in such effects as those arising from geometric orientations and subtle physical processes at the explosion. SNe with more complete nuclear burning, which converts Si to Fe group elements, show shallower Si II lines (see Figure 9, right panel). At the luminous end, with $\Delta m_{15} \lesssim 1$, the light-curve shape is insensitive to these effects but the luminosity is correlated with the strength of the Si II 6355 line (see Figure 10). In the context of delayed detonation, this may be further related to the central density at ignition and the mass of the progenitors (Khokhlov 1991; Khokhlov et al. 1993; Höflich et al. 1996; Hoeflich et al. 2017). Quantitative modeling of these physical processes is beyond the scope of this study. If geometric effect dominates the observed luminosity and Si II 6355 line strength correlation, Figure 10 suggests that the side with more advanced nuclear burning shows weaker Si II lines when faced with the observer. The geometry of SNe Ia has been probed by

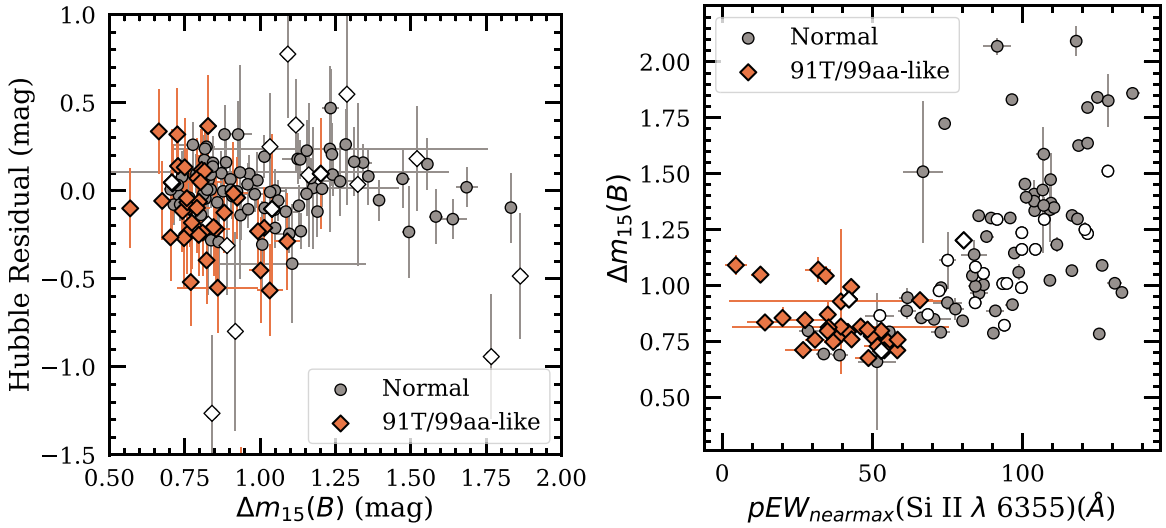

Figure 9. Left: Hubble residual vs. $\Delta m_{15}(B)$. Right: $\Delta m_{15}(B)$ vs. $pEW_{\rm max}$(Si II $\lambda\lambda$6355). Open circles indicate objects with $z_{\rm CMB}$<0.01.

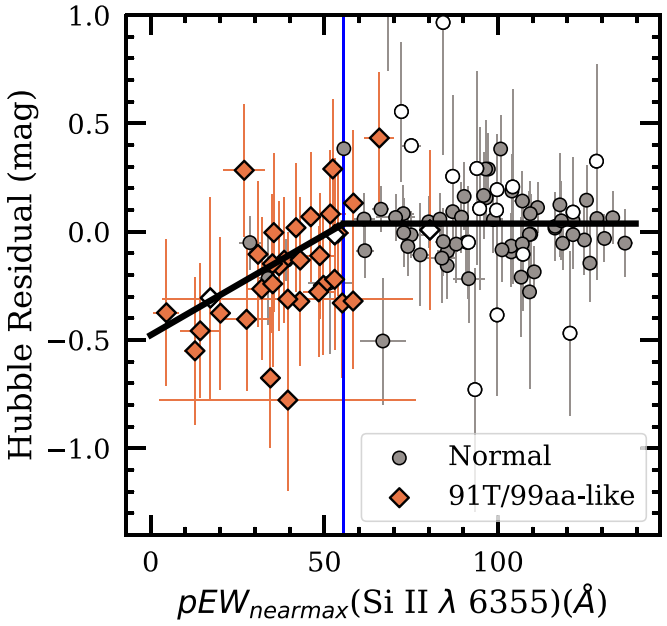

Figure 10. Hubble residual vs. $pEW_{\rm max}$(SiII$\lambda\lambda$6355). Open circles indicate objects with $z_{\rm cmb} < 0.01$. Blue vertical line in the right panel is where pEW = 55.62 Å. Black line in the right panel shows the best linear fit for objects with pEW < 55.62 Å (Hubble residual (mag) = 0.009 × $pEW_{\rm max}$ Si IIλ6355(Å)−0.482), and the weighted mean (= 0.036 mag) for objects with pEW > 55.62 Å.

spectropolarimetry, and the degree of continuum polarization is consistently low ($\lesssim$0.2%). The level of Si II 6355 line polarization is around 0.5% in general (Wang et al. 2008; Cikota et al. 2019; Yang et al. 2020). There have been no published spectropolarimetry data that can place tight constraints on the geometric shapes of the 91T/99aa-like events, although recent data seem to indicate that they are very lowly polarized similar to other SNe Ia (Y. Yang, private communication, 2022). If geometric effect does play a role, spectroscopy during the late-time nebular phase can also be of great diagnostic value. Interestingly, these observations are qualitatively consistent with the discovery that SNe with larger light-curve stretch values are both more luminous and less polarized (Wang et al. 2008; Cikota et al. 2019). The more complete burning effectively removes the asymmetries arising from the instabilities during the deflagration phase preceding the detonation.

This work is enabled by observations made from the Las Cumbres Observatory Global Telescope network. The Las Cumbres Observatory team is supported by NSF grants AST-1911225 and AST-1911151. This work also used the computing resources provided by Texas A&M High Performance Research Computing. J.Y. acknowledges generous support from the Texas A&M University and the George P. and Cynthia Woods Institute for Fundamental Physics and Astronomy. We thank the Mitchell Foundation for their support of the Cook's Branch meetings on Supernovae. We thank Mark Phillips for discussions early on in this project pertaining to the over luminosity of 91T-like SNe Ia in the Hubble diagram and the relationship between the Hubble residual and the pEW_{max}(*Si II* $\lambda\lambda$6355). J.Y. also thanks Yi Yang, Xiaofeng Wang, and Chris Burns for helpful discussion. J.Y. acknowledges the generosity of Nikolaus Volgenau in helping us understand the Las Cumbres telescopes. L.W. is supported by NSF grant AST-1817099. P.J.B. is supported by NASA grant 80NSSC20K0456, "SOUSA's Sequel: Improving Standard Candles by Improving UV Calibration." L.G. acknowledges financial support from the Spanish Ministerio de Ciencia e Innovación (MCIN), the Agencia Estatal de Investigación (AEI) 10.13039/501100011033, and the European Social Fund (ESF) "Investing in your future" under the 2019 Ramón y Cajal program RYC2019-027683-I and the PID2020-115253GA-I00 HOSTFLOWS project, from Centro Superior de Investigaciones Científicas (CSIC) under the PIE project 20215AT016, and the program Unidad de Excelencia María de Maeztu CEX2020-001058-M. This work is supported by NSF through the grant AST-1613455 to N.S.

ORCID iDs

Jiawen Yang https://orcid.org/0000-0002-1376-0987
Lifan Wang https://orcid.org/0000-0001-7092-9374
Nicholas Suntzeff https://orcid.org/0000-0002-8102-181X
Lei Hu https://orcid.org/0000-0001-7201-1938
Lauren Aldoroty https://orcid.org/0000-0003-0183-451X

Peter J. Brown https://orcid.org/0000-0001-6272-5507
Kevin Krisciunas https://orcid.org/0000-0002-6650-694X
Iair Arcavi https://orcid.org/0000-0001-7090-4898
Jamison Burke https://orcid.org/0000-0003-0035-6659
Lluís Galbany https://orcid.org/0000-0002-1296-6887
Daichi Hiramatsu https://orcid.org/0000-0002-1125-9187
Griffin Hosseinzadeh https://orcid.org/0000-0002-0832-2974
D. Andrew Howell https://orcid.org/0000-0003-4253-656X
Curtis McCully https://orcid.org/0000-0001-5807-7893
Craig Pellegrino https://orcid.org/0000-0002-7472-1279
Stefano Valenti https://orcid.org/0000-0001-8818-0795

References

Altavilla, G., Fiorentino, G., Marconi, M., et al. 2004, MNRAS, 349, 1344
Baltay, C., Grossman, L., Howard, R., et al. 2021, PASP, 133, 44002
Benetti, S., Cappellaro, E., Mazzali, P. A., et al. 2005, ApJ, 623, 1011
Bertin, E., Mellier, Y., Radovich, M., et al. 2002, in ASP Conf. Ser. 281, Astronomical Data Analysis Software and Systems XI, ed. D. A. Bohlender, D. Durand, & T. H. Handley (San Francisco, CA: ASP), 228
Bessell, M. S. 1990, PASP, 102, 1181
Betoule, M., Kessler, R., Guy, J., et al. 2014, A&A, 568, A22
Blondin, S., Matheson, T., Kirshner, R. P., et al. 2012, AJ, 143, 126
Boone, K., Aldering, G., Antilogus, P., et al. 2021, ApJ, 912, 71
Branch, D., Dang, L. C., Hall, N., et al. 2006, PASP, 118, 560
Brown, P. J., Breeveld, A. A., Holland, S., Kuin, P., & Pritchard, T. 2014, A&SS, 354, 89
Brown, T. M., Baliber, N., Bianco, F. B., et al. 2013, PASP, 125, 1031
Burns, C. R., Stritzinger, M., Phillips, M. M., et al. 2011, AJ, 141, 19
Burrow, A., Baron, E., Ashall, C., et al. 2020, ApJ, 901, 154
Childress, M., Aldering, G., Antilogus, P., et al. 2013, ApJ, 770, 108
Cikota, A., Patat, F., Wang, L., et al. 2019, MNRAS, 490, 578
Conley, A., Carlberg, R. G., Guy, J., et al. 2007, ApJL, 664, L13
Daddi, E., Dickinson, M., Morrison, G., et al. 2007, ApJ, 670, 156
DePoy, D. L., Atwood, B., Belville, S. R., et al. 2003, Proc. SPIE, 4841, 827
Elbaz, D., Daddi, E., Le Borgne, D., et al. 2007, A&A, 468, 33
Filippenko, A. V., Richmond, M. W., Branch, D., et al. 1992b, AJ, 104, 1543
Filippenko, A. V., Richmond, M. W., Matheson, T., et al. 1992a, ApJL, 384, L15
Fitzpatrick, E. L. 1999, PASP, 111, 63
Fitzpatrick, E. L., & Massa, D. 1999, ApJ, 525, 1011
Foley, R. J., Scolnic, D., Rest, A., et al. 2018, MNRAS, 475, 193
Freedman, W. L., Madore, B. F., Gibson, B. K., et al. 2001, ApJ, 553, 47
Fukugita, M., Ichikawa, T., Gunn, J. E., et al. 1996, AJ, 111, 1748
Ganeshalingam, M., Li, W., Filippenko, A. V., et al. 2010, ApJS, 190, 418
Garavini, G., Folatelli, G., Goobar, A., et al. 2004, AJ, 128, 387
Goldhaber, G., Groom, D. E., Kim, A., et al. 2001, ApJ, 558, 359
Goobar, A., & Perlmutter, S. 1995, ApJ, 450, 14
Guillochon, J., Parrent, J., Kelley, L. Z., & Margutti, R. 2017, ApJ, 835, 64
Gupta, R. R., D'Andrea, C. B., Sako, M., et al. 2011, ApJ, 740, 92
Guy, J., Astier, P., Baumont, S., et al. 2007, A&A, 466, 11
Guy, J., Sullivan, M., Conley, A., et al. 2010, A&A, 523, A7
Hakobyan, A. A., Barkhudaryan, L. V., Karapetyan, A. G., et al. 2020, MNRAS, 499, 1424
Hamuy, M. 2003, ApJ, 582, 905
Hamuy, M., Phillips, M. M., Suntzeff, N. B., et al. 1996a, AJ, 112, 2398
Hamuy, M., Phillips, M. M., Suntzeff, N. B., et al. 1996b, AJ, 112, 2391
Hamuy, M., Phillips, M. M., Wells, L. A., & Maza, J. 1993, PASP, 105, 787
He, S., Wang, L., & Huang, J. Z. 2018, ApJ, 857, 110
Henden, A. A., Templeton, M., Terrell, D., et al. 2016, yCat, 2336, II/336
Hicken, M., Challis, P., Jha, S., et al. 2009, ApJ, 700, 331
Hicken, M., Challis, P., Kirshner, R. P., et al. 2012, ApJS, 200, 12
Hoeflich, P., Hsiao, E. Y., Ashall, C., et al. 2017, ApJ, 846, 58
Höflich, P., Khokhlov, A., Wheeler, J. C., et al. 1996, ApJL, 472, L81
Howell, D. A., Sullivan, M., Nugent, P. E., et al. 2006, Natur, 443, 308
Hsiao, E. Y., Conley, A., Howell, D. A., et al. 2007, ApJ, 663, 1187
Hu, L., Chen, X., & Wang, L. 2022, ApJ, 930, 70
Hu, L., Wang, L., Chen, X., & Yang, J. 2021, ApJ, 936, 157
Iben, I., Jr., & Tutukov, A. V. 1984, ApJs, 54, 335
Jha, S., Kirshner, R. P., Challis, P., et al. 2006, AJ, 131, 527
Johansson, J., Thomas, D., Pforr, J., et al. 2013, MNRAS, 435, 1680
Jordi, K., Grebel, E. K., & Ammon, K. 2006, A&A, 460, 339
Kelly, P. L., Hicken, M., Burke, D. L., Mandel, K. S., & Kirshner, R. P. 2010, ApJ, 715, 743
Khokhlov, A., Mueller, E., & Hoeflich, P. 1993, A&A, 270, 223
Khokhlov, A. M. 1991, A&A, 245, 114
Kim, A., Goobar, A., & Perlmutter, S. 1996, PASP, 108, 190
Krisciunas, K., Contreras, C., Burns, C. R., et al. 2017, AJ, 154, 211
Krisciunas, K., Hastings, N. C., Loomis, K., et al. 2000, ApJ, 539, 658
Krisciunas, K., Suntzeff, N. B., Candia, P., et al. 2003, AJ, 125, 166
Lampeitl, H., Smith, M., Nichol, R. C., et al. 2010, ApJ, 722, 566
Léget, P. F., Gangler, E., Mondon, F., et al. 2020, A&A, 636, A46
Leibundgut, B., Kirshner, R. P., Phillips, M. M., et al. 1993, AJ, 105, 301
Li, W., Filippenko, A. V., Chornock, R., et al. 2003, PASP, 115, 453
Li, W., Filippenko, A. V., Treffers, R. R., et al. 2001, ApJ, 546, 734
Lineweaver, C. H. 1997, in 16th Moriond Astrophysics Meeting: Microwave Background Anisotropies (College Park, MD: AIP), 69
Lira, P., Suntzeff, N. B., Phillips, M. M., et al. 1998, AJ, 115, 234
McCully, C., Volgenau, N. H., Harbeck, D.-R., et al. 2018, Proc. SPIE, 10707, 107070K
Noeske, K. G., Weiner, B. J., Faber, S. M., et al. 2007, ApJL, 660, L43
Perlmutter, S., Aldering, G., Goldhaber, G., et al. 1999, ApJ, 517, 565
Phillips, M. M. 1993, ApJL, 413, L105
Phillips, M. M., Contreras, C., Hsiao, E. Y., et al. 2019, PASP, 131, 14001
Phillips, M. M., Lira, P., Suntzeff, N. B., et al. 1999, AJ, 118, 1766
Phillips, M. M., Wells, L. A., Suntzeff, N. B., et al. 1992, AJ, 103, 1632
Press, W. H., Teukolsky, S. A., Vetterling, W. T., & Flannery, B. P. 2007, Numerical Recipes 3rd Edition: The Art of Scientific Computing (3rd edn.; Cambridge: Cambridge Univ. Press)
Reindl, B., Tammann, G. A., Sandage, A., & Saha, A. 2005, ApJ, 624, 532
Riess, A. G., Casertano, S., Yuan, W., Macri, L. M., & Scolnic, D. 2019, ApJ, 876, 85
Riess, A. G., Filippenko, A. V., Challis, P., et al. 1998, AJ, 116, 1009
Riess, A. G., Kirshner, R. P., Schmidt, B. P., et al. 1999, AJ, 117, 707
Riess, A. G., Press, W. H., & Kirshner, R. P. 1996, ApJ, 473, 88
Riess, A. G., Yuan, W., Macri, L. M., et al. 2021, ApJL, 934, L7
Saunders, C., Aldering, G., Antilogus, P., et al. 2018, ApJ, 869, 167
Scalzo, R., Aldering, G., Antilogus, P., et al. 2012, ApJ, 757, 12
Schlegel, D. J., Finkbeiner, D. P., & Davis, M. 1998, ApJ, 500, 525
Silverman, J. M., Foley, R. J., Filippenko, A. V., et al. 2012, MNRAS, 425, 1789
Smitka, M. T., Brown, P. J., Suntzeff, N. B., et al. 2015, ApJ, 813, 30
Stahl, B. E., Zheng, W., de Jaeger, T., et al. 2019, MNRAS, 490, 3882
Stetson, P. B. 1987, PASP, 99, 191
Stritzinger, M., Hamuy, M., Suntzeff, N. B., et al. 2002, AJ, 124, 2100
Strolger, L. G., Smith, R. C., Suntzeff, N. B., et al. 2002, AJ, 124, 2905
Sullivan, M., Conley, A., Howell, D. A., et al. 2010, MNRAS, 406, 782
Suntzeff, N. B., Phillips, M. M., Covarrubias, R., et al. 1999, AJ, 117, 1175
Taam, R. E. 1980, ApJ, 237, 142
Tripp, R. 1998, A&A, 331, 815
Uddin, S. A., Burns, C. R., Phillips, M. M., et al. 2020, ApJ, 901, 143
Valenti, S., Howell, D. A., Stritzinger, M. D., et al. 2016, MNRAS, 459, 3939
Wagers, A., Wang, L., & Asztalos, S. 2010, ApJ, 711, 711
Wang, X., Filippenko, A. V., Ganeshalingam, M., et al. 2009, ApJL, 699, L139
Wang, X., Li, W., Filippenko, A. V., et al. 2008, ApJ, 675, 626
Webbink, R. F. 1984, ApJ, 277, 355
Whelan, J., & Iben, I., Jr. 1973, ApJ, 186, 1007
Woosley, S. E., & Weaver, T. A. 1994, ApJ, 423, 371
Yang, Y., Hoeflich, P., Baade, D., et al. 2020, ApJ, 902, 46
Zhang, J.-J., Wang, X.-F., Sasdelli, M., et al. 2016, ApJ, 817, 114